Earth System Model Aerosol-Cloud Diagnostics Package (ESMAC Diags) Version 2: Assessments of Aerosols, Clouds and Aerosol-Cloud Interactions Through Field Campaign and Long-Term Observations

Shuaiqi Tang[1], Adam C. Varble[1], Jerome D. Fast[1], Kai Zhang[1], Peng Wu[1], Xiquan Dong[2], Fan Mei[1], Mikhail Pekour[1], Joseph C. Hardin[3], and Po-Lun Ma[1]

[1]Pacific Northwest National Laboratory, Richland, WA, USA
[2]University of Arizona, Tucson, AZ, USA
[3]Unaffiliated scientist

Correspondence to: Shuaiqi Tang (shuaiqi.tang@pnnl.gov)

Abstract.

Poor representations of aerosols, clouds and aerosol-cloud interactions (ACI) in Earth System Models (ESMs) have long been the largest uncertainties in predicting global climate change. Huge efforts have been made to improve the representation of these processes in ESMs, and key to these efforts is evaluation of ESM simulations with observations. Most well-established ESM diagnostics packages focus on the climatological features; however, they are lacking process-level understanding and representations of aerosols, clouds, and ACI. In this study, we developed an ESM aerosol-cloud diagnostics package (ESMAC Diags) to facilitate routine evaluation of aerosols, clouds and aerosol-cloud interactions simulated by the Department of Energy's (DOE) Energy Exascale Earth System Model (E3SM). This paper documents its version 2 functionality (ESMAC Diags v2), which has substantial updates from its version 1 (Tang et al., 2022a). The simulated aerosol and cloud properties have been extensively compared with in-situ and remote-sensing measurements from aircraft, ship, surface and satellite platforms in ESMAC Diags v2. It currently includes six field campaigns and two permanent sites covering four geographical regions: Eastern North Atlantic, Central U.S., Northeastern Pacific and Southern Ocean, where frequent liquid or mixed-phase clouds are present and extensive measurements are available from the DOE Atmospheric Radiation Measurement user facility and other agencies. ESMAC Diags v2 generates various types of single-variable and multi-variable diagnostics, including percentiles, histograms, joint histograms and heatmaps, to evaluate model representation of aerosols, clouds, and ACI. Select examples highlighting ESMAC Diags capabilities are shown using E3SM version 2 (E3SMv2). E3SMv2 in general can reasonably reproduces many observed aerosol and cloud properties, with biases in some variables such as aerosol particle and cloud droplet sizes and number concentrations. The coupling of aerosol and cloud number concentrations may be too strong in E3SMv2, possibly indicating a bias in processes that control aerosol activation. Furthermore, the liquid water path response to perturbed cloud droplet number concentration behaves differently in E3SMv2 and observations, which warrants a further study to improve the cloud microphysics parameterizations in E3SMv2.

1. Introduction

Poor representations of aerosols, clouds and aerosol-cloud interactions (ACI) in Earth System Models (ESMs) have long been the largest uncertainties in predicting global climate change (Ipcc, 2021). Challenges come from several aspects: first, there are many aerosol properties (e.g., number, size, phase, shape, composition) and cloud micro- and macro-physical properties (e.g., fraction, water content, number and size of liquid and ice hydrometeors) that affect Earth's climate. Coincident measurements of these properties remain largely under-sampled due to substantial spatiotemporal variability and logistical difficulties for making such measurements. Second, there are complex interactive processes between aerosols, clouds, and ambient meteorological conditions, many of which are not fully understood, but are critical to properly interpreting relationships between observable properties. Third, many ACI processes are nonlinear, multi-scale processes that involve feedbacks depending on cloud types and meteorological regimes, which also shift in space and time, presenting challenges for assessing causal effect and representing such processes in ESMs.

Huge efforts have been made to improve the representation of aerosols, clouds and ACI in ESMs. Key to these efforts is evaluation of ESM simulations with observations. Many modeling centers have developed standardized diagnostics packages to document ESM performance. For aerosol and cloud properties, most diagnostic packages rely heavily on satellite measurements as evaluation data (e.g., Amwg, 2021; E3sm, 2021; Eyring et al., 2016; Gleckler et al., 2016; Maloney et al., 2019; Myhre et al., 2013; Schulz et al., 2006). Satellite remote sensing measurements have global or near global coverage but limited spatial and temporal resolution. They are also facing many challenges to retrieve some variables, especially for aerosol properties such as number concentration, size distribution, chemical composition etc. Some recent studies (e.g., Choudhury and Tesche, 2022) have retrieved cloud condensation nuclei (CCN) number concentration from satellite measurements, which provides a great addition to investigate ACI in global scale. However, large uncertainties exist in satellite retrievals, even for more sophisticated retrieved cloud microphysical properties such as droplet number concentration (e.g., Grosvenor et al., 2018). This limits their application to robustly quantify aerosols, clouds and ACI processes. In-situ measurements from ground, aircraft or ship platforms from field campaigns are also used in a few projects to evaluate ESMs (e.g., Reddington et al., 2017; Watson-Parris et al., 2019; Tang et al., 2022a; Zhang et al., 2020). Some of these field campaigns were conducted over remote or poorly sampled locations, which are highly valuable for model evaluation despite limited spatial coverage and time periods. Moreover, the U.S. Department of Energy (DOE) Atmospheric Radiation Measurement (ARM) user facility has conducted continuous field measurements at a few sites for multiple years. These long-term high-resolution field measurements have also been demonstrated to be valuable for evaluating ESMs (e.g., Zhang et al., 2020).

In response to the need for more ESM diagnostics for evaluating ACI processes, Tang et al. (2022a) developed an ESM aerosol-cloud diagnostics package (ESMAC Diags) to facilitate the routine evaluation of aerosols, clouds and ACI simulated by the Department of Energy's (DOE) Energy Exascale Earth System Model (E3SM, Golaz et al., 2019). It includes diagnostics that leverage in-situ measurements from multiple platforms during six field campaigns since 2013, which are not included in previous diagnostics tools (e.g., Reddington et al., 2017). Version 1 of ESMAC Diags (ESMAC Diags v1, Tang et al., 2022a) mainly focuses on aerosol properties. We present here version 2 of ESMAC Diags (ESMAC Diags v2) that is a direct extension of ESMAC Diags v1 with two major additions:

1. measurements from satellite and long-term diagnostics at the ARM Southern Great Plains (SGP) and Eastern North Atlantic (ENA) sites.

2. diagnostics for cloud properties and aerosol-cloud interactions.

The new measurements, as well as major data quality controls are introduced in Section 2. Additional discussions on retrieval uncertainties of cloud microphysical properties are performed in Section 3. Details of the code structure of ESMAC Diags v2, which is substantially changed since version 1, are described in Section 4. Section 5 provides selected examples of single-variable and multi-variable diagnostics using ESMAC Diags v2 to highlight its capabilities. Lastly, Section 6 provides a summary.

2. Aerosol and cloud measurements from ground, aircraft, ship and satellite platforms

Following the initial development in version 1, ESMAC Diags v2 continues to focus on six field campaigns conducted in four geographical regions: the Central U.S. (CUS, where the ARM Southern Great Plains (SGP) site is located), Eastern North Atlantic (ENA), Northeastern Pacific (NEP), and Southern Ocean (SO). Information on the six field campaigns is shown in Table 1 and their locations are shown in Figure 1, each reproduced from Table 1 and Figure 3 in Tang et al. (2022a).

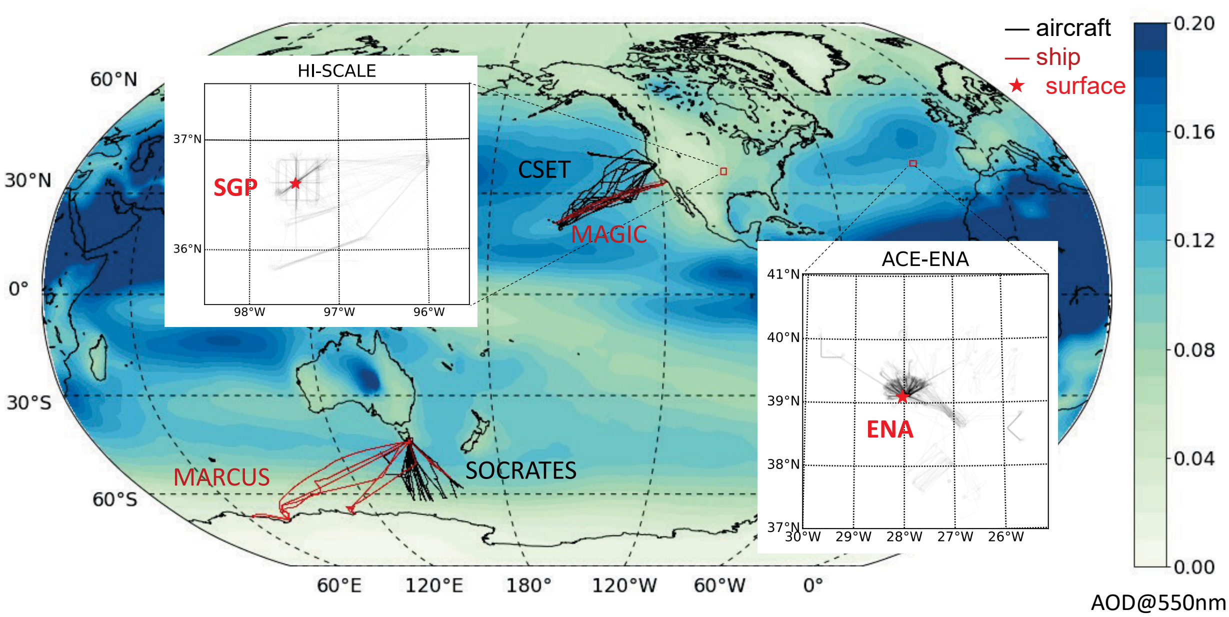

Figure 1. Aircraft (black) and ship (red) tracks for the six field campaigns. Red stars in the enlarged map indicate two ARM fixed sites: SGP and ENA, that have long-term measurements available for model diagnostics. Overlaid is aerosol optical depth at 550nm averaged from 2014 to 2018 simulated in E3SMv1. (Reproduced from Figure 3 in Tang et al., 2022a)

Table 1. Descriptions of the field campaigns used in this study. (Reproduced from Table 1 in Tang et al., 2022a)

Campaign*	Period	Platform	Typical Conditions	Reference

HI-SCALE	IOP1: 24 Apr – 21 May 2016 IOP2: 28 Aug – 24 Sep 2016	Ground, aircraft (IOP1: 17 flights, IOP2: 21 flights)	Continental cumulus with high aerosol loading	(Fast et al., 2019)
ACE-ENA	IOP1: 21 Jun – 20 Jul 2017 IOP2: 15 Jan – 18 Feb 2018	Ground, aircraft (IOP1: 20 flights, IOP2: 19 flights)	Marine stratocumulus with low aerosol loading	(Wang et al., 2021)
MAGIC	Oct 2012 – Sep 2013	Ship (18 legs)	Marine stratocumulus to cumulus transition with low aerosol loading	(Lewis and Teixeira, 2015; Zhou et al., 2015)
CSET	1 Jul – 15 Aug 2015	Aircraft (16 flights)	Same as above	(Albrecht et al., 2019)
MARCUS	Oct 2017 – Apr 2018	Ship (4 legs)	Marine liquid and mixed phase clouds with low aerosol loading	(Mcfarquhar et al., 2021)
SOCRATES	15 Jan – 24 Feb, 2018	Aircraft (14 flights)	Same as above	(Mcfarquhar et al., 2021)

* Full names of the listed field campaigns:
HI-SCALE: Holistic Interactions of Shallow Clouds, Aerosols and Land Ecosystems
ACE-ENA: Aerosol and Cloud Experiments in the Eastern North Atlantic
MAGIC: Marine ARM GCSS Pacific Cross-section Intercomparison (GPCI) Investigation of Clouds
CSET: Cloud System Evolution in the Trades
MARCUS: Measurements of Aerosols, Radiation and Clouds over the Southern Ocean
SOCRATES: Southern Ocean Cloud Radiation and Aerosol Transport Experimental Study

The collection and processing of observations are the most time-consuming part of developing ESMAC Diags, which also impacts the reliability of conclusions drawn from the model diagnostics. In this section, we introduce the data used in ESMAC Diags v2, existing quality issues in some datasets, and treatments to address these quality issues. Some variables are difficult to directly measure or have limited in-situ sampling and thus must be derived from remote sensing measurements using retrieval algorithms. In Section 3, we further discuss the uncertainty and reliability of some cloud retrieval products via comparisons with in-situ aircraft measurements.

2.1. Data availability

All measurements, instruments, and data products used in the six field campaigns and two long-term sites in ESMAC Diags v2 are shown in Table 2. Further details of the measurements, data product names, and DOIs are given in Tables S1 to S6 (for field campaigns) and Tables S7 and S8 (for SGP and ENA sites) in the supplementary material. To allow maximum overlapping of key measurements while also ensuring a long enough period for statistical evaluation, we select the periods of 1 Jan 2011 – 31 Dec 2020 for SGP and 1 Jan 2016 – 31 Dec 2018 for ENA for long-term analyses. In addition to the aerosol measurements discussed in Tang et al. (2022a), we incorporate more cloud and radiation measurements, as well as geostationary satellite retrievals using Visible Infrared Solar-Infrared Split Window Technique (VISST) (Minnis et al., 2008; Minnis et al., 2011) algorithm. The VISST products archived by ARM cover approximately 10° by 10° regions in 0.5° by 0.5° resolution centered over ARM sites. Moreover, ARM recently released products consisting of merged aerosol particle and cloud droplet size distributions from aircraft measurements for HI-SCALE and ACE-ENA campaigns. These data are now used in ESMAC Diags v2.

Table 2: List of instruments and measurements used in ESMAC Diags v2.

Platform	Measurements	Instruments / data products	Available campaigns
Ground	Surface temperature, relative humidity, wind, pressure, precipitation; upper-level temperature, relative humidity, wind	Surface meteorological station (MET), ARM best estimate (ARMBE) products	HI-SCALE, ACE-ENA, SGP, ENA
	Longwave and shortwave radiation, cloud fraction	ARM best estimate (ARMBE) products	HI-SCALE, ACE-ENA, SGP, ENA
	Aerosol number concentration	Condensation particle counter (CPC), Condensation particle counter – fine (CPCF), Condensation particle counter – ultrafine (CPCU), Ultra-high sensitivity aerosol spectrometer (UHSAS), Scanning mobility particle sizer (SMPS)	HI-SCALE, ACE-ENA, SGP, ENA
	Aerosol size distribution	Ultra-high sensitivity aerosol spectrometer (UHSAS), Scanning mobility particle sizer (SMPS), Nano scanning mobility particle sizer (nanoSMPS)	HI-SCALE, ACE-ENA, SGP, ENA
	Aerosol composition	Aerosol chemical speciation monitor (ACSM)	HI-SCALE, ACE-ENA, SGP, ENA
	CCN number concentration	Cloud condensation nuclei (CCN) counter	HI-SCALE, ACE-ENA, SGP, ENA
	Cloud optical depth	Multifilter rotating shadowband radiometer (MFRSR)	HI-SCALE, ACE-ENA, SGP, ENA
	Cloud droplet number concentration	Cloud droplet number concentration retrieval (Ndrop), cloud retrieval from Wu et al. (2020)	HI-SCALE, ACE-ENA, SGP, ENA
	Cloud droplet effective radius	Multifilter rotating shadowband radiometer (MFRSR), cloud retrieval from Wu et al. (2020)	HI-SCALE, ACE-ENA, SGP, ENA
	Cloud liquid water path	Microwave radiometer (MWR), ARM best estimate (ARMBE) products	HI-SCALE, ACE-ENA, SGP, ENA
	Cloud base height, cloud top height	Active remote sensing of clouds (ARSCL)	HI-SCALE, ACE-ENA, SGP, ENA
Satellite	TOA shortwave and longwave radiation	Geostationary satellite-based retrievals using Visible Infrared Solar-Infrared Split Window Technique (VISST) algorithm	HI-SCALE, ACE-ENA, MAGIC, MARCUS, SGP, ENA
	cloud fraction; height, pressure and temperature at cloud top	Geostationary satellite-based retrievals using Visible Infrared Solar-Infrared Split Window Technique (VISST) algorithm	HI-SCALE, ACE-ENA, MAGIC, MARCUS, SGP, ENA
	liquid water path; cloud optical depth; droplet effective radius	Geostationary satellite-based retrievals using Visible Infrared Solar-Infrared Split Window Technique (VISST) algorithm	HI-SCALE, ACE-ENA, MAGIC, MARCUS, SGP, ENA
	Cloud droplet number concentration	Retrieved from VISST data using the algorithm in Bennartz (2007)	HI-SCALE, ACE-ENA, MAGIC, MARCUS, SGP, ENA
Aircraft	Navigation information and meteorological parameters	Interagency working group for airborne data and telemetry systems (IWG)	HI-SCALE, ACE-ENA
	Aerosol number concentration	Condensation particle counter (CPC), Condensation particle counter – ultrafine (CPCU), Condensation nuclei counter (CNC), Ultra-high sensitivity aerosol spectrometer (UHSAS), Passive cavity aerosol spectrometer (PCASP)	HI-SCALE, ACE-ENA, CSET, SOCRATES

	Aerosol size distribution	Ultra-high sensitivity aerosol spectrometer (UHSAS), Fast integrated mobility spectrometer (FIMS), Passive cavity aerosol spectrometer (PCASP), Best estimate aerosol size distribution (BEASD)	HI-SCALE, ACE-ENA, CSET, SOCRATES
	Aerosol composition	High-resolution time-of-flight aerosol mass spectrometer (AMS)	HI-SCALE, ACE-ENA
	CCN number concentration	Cloud condensation nuclei (CCN) counter	HI-SCALE, ACE-ENA, SOCRATES
	Cloud liquid water content	Water content measuring system (WCM), PMS-King Liquid Water Content (LWC)	HI-SCALE, ACE-ENA, CSET, SOCRATES
	Cloud droplet number size distribution	1DC, 2DC, 2DS, CDP, Cloud probe merged size distribution (mergedSD)	HI-SCALE, ACE-ENA, CSET, SOCRATES
Ship	Navigation information and meteorological parameters	Meteorological station (MET)	MAGIC, MARCUS
	Aerosol number concentration	Condensation particle counter (CPC), Ultra-high sensitivity aerosol spectrometer (UHSAS)	MAGIC, MARCUS
	Aerosol size distribution	Ultra-high sensitivity aerosol spectrometer (UHSAS)	MAGIC, MARCUS
	CCN number concentration	Cloud condensation nuclei (CCN) counter	MAGIC, MARCUS
	Cloud liquid water path	Microwave radiometer (MWR)	MAGIC, MARCUS
	Cloud droplet number concentration, cloud effective radius	Cloud retrieval from Wu et al. (2020)	MAGIC

All the observational data are quality controlled with their time resolution re-scaled to that suitable for evaluating E3SM, and the rescale resolution can be adjusted to fit for different model output frequencies. Currently, ground, ship and satellite measurements are re-scaled to a 1-hour frequency to be consistent with current E3SM output frequency. Rescaling consists of computing either the median, mean or interpolated value depending on the original data frequency and variable properties. For most aerosol and cloud microphysics measurements, the median value is computed to remove occasional spikes or zeros resulting from data contamination or measurement error. For some bulk cloud properties (e.g., cloud fraction, liquid water path (LWP)), the mean value is computed to be consistent with grid-mean E3SM output. Interpolation is only used when the input frequency is equal to or coarser than the frequency of model output. For aircraft measurements, 1-minute resolution is used to retain high variability and allow matching samples of aerosol and cloud at the same time. To compare with high-frequency aircraft data, E3SM output is interpolated to the same resolution using the nearest grid cell and time slice. Although the current 1-hour, 1-degree E3SM output could not capture the high variability of the aircraft measurements, we are targeting the exascale E3SM version planned in the next few years. In kilometer scale resolution ESM simulations, the high variability in aircraft measurements will be better captured. In the current diagnostics we only focus on the statistics for the entire campaign. As seen later in Section 5.1, coarse-resolution model outputs show similar percentile ranges with the high-resolution aircraft measurements, indicating that for simple percentiles, large-scale variabilities dominate over subgrid variabilities over month-long field campaign periods. Further analysis is needed to understand the importance of other statistics (variance, covariance, etc.) of subgrid scale variabilities. . All processed data are saved in a standardized NetCDF format (Netcdf, 2022) and available for downloading (see data availability section) and direct use.

2.2 Data quality issues and treatments

Many observation datasets used in ESMAC Diags are ARM level-b (quality-controlled) or level-c (value-added) products, which include quality control (QC) flags to indicate data quality issues. For most datasets, a QC treatment is applied to remove all data with questionable flags. However, there are certain datasets or circumstances in which a QC flag is overly strict (too many good data are removed) or not strict enough (some bad data are not removed). Here we document some of these situations and how we handle them in our data processing.

2.2.1 ARM Condensation Particle Counter (CPC) measurements

ARM CPC data have several QC values representing failure of different quality checks. One of them checks if the concentration is greater than a maximum allowable value, which is set to 8,000 cm^{-3} for model 3010 (CPC, size detection limit 10 nm), 10,000 cm^{-3} for model 3772 (CPCF, size detection limit 10 nm), and 50,000 cm^{-3} for model 3776 (CPCU, size detection limit 3 nm). At SGP, new particle formation (NPF) events occur frequently when CPC and CPCF measurements can exceed 30,000 cm^{-3}. This is much higher than the maximum allowable value but physically reasonable. Simply removing these large values results in an underestimation of aerosol number concentration and produces unrealistic diurnal cycle since they usually occur during the daytime (Tang et al., 2022a). By consulting with the ARM instrument mentor, we only remove data with critical QC flags, but keep data with this QC flag that is overly restrictive.

2.2.2 NCAR research flight aerosol number concentration (CN) measurements

NCAR research flight (RF) data used in ESMAC Diags do not include QC flags but occasionally show suspiciously large or negative aerosol counts. The following minimum and maximum thresholds are applied to remove suspicious data:

- Total CN from a Condensation Nucleation Counter (CNC, reported as CONCN): minimum = 0, maximum = 25,000 cm^{-3}.
- Total CN from an Ultra-High-Sensitivity Aerosol Spectrometer (UHSAS, reported as UHSAS100): minimum = 0, maximum = 5,000 cm^{-3}.
- Aerosol number size distribution from an UHSAS (reported as CUHSAS_RWOOU or CUHSAS_LWII): minimum = 0, maximum = 500 cm^{-3} per size bin.

2.2.3 Ship-measured aerosol properties

Aerosol instruments on ships are occasionally contaminated by ship emissions, which present as large spikes in aerosol and CCN number concentrations. For ARM MARCUS measurements, Humphries (2020) published reprocessed CN and CCN data to remove ship exhaust contamination using method described in Humphries et al. (2019). This data is used in this diagnostics package. For MAGIC, we could not find any ship exhaust contamination information. By visually examining the dataset, a simple maximum threshold (25,000 cm^{-3} for CPC, 5,000 cm^{-3} for UHSAS100, 2,000 cm^{-3} for CCN at 0.1% supersaturation and 4,000 cm^{-3} for CCN at 0.5% supersaturation) is applied to remove likely contamination from ship emissions.

2.2.4 CCN measurements

There are different supersaturation (SS) setting strategies for CCN measurements. Some aircraft campaigns measured CCN with constant SS (ACE-ENA, HI-SCALE). Some other campaigns measured CCN with time-varying (scanning) SS (SOCRATES, surface CCN counters at SGP and ENA). However, the actual SS in a scanning strategy has fluctuations that are different than the target SS. For the latter, CCN for each SS (0.1%, 0.2%, 0.3% and 0.5%) are obtained by selecting CCN measured within ± 0.05% of the SS target.

For long-term measurements at SGP and ENA, near-hourly CCN spectra data are available, and a quadratic polynomial is fit to the spectra such that CCN number concentration can be estimated at any SS between the measured minimum and maximum SS values. We calculate and output CCN number concentration from these fits at three target supersaturations (0.1%, 0.2% and 0.5%). The fitted spectra data provides CCN number concentration at the exact target supersaturations, but the sample number is slightly smaller due to occasional failure of polynomial fitting.

2.2.5 Contaminated surface aerosol measurements at ENA

The ARM ENA site is located at a local airport. Aerosol measurements at ENA are sometimes contaminated by aircraft and vehicle emissions, rendering the measurements not representative of the background environment. Gallo et al. (2020) identified periods when CPC measurements were likely contaminated from localized emissions (Figure 2a). Their aerosol mask data has 1-min resolution. When we rescale the data to 1-hr resolution and apply the mask on other coarse time-resolution aerosol measurements (e.g., ACSM, Figure 2c), we mask hours in which more than half of the hour is flagged by the aerosol mask. The masking slightly increases the occurrence fraction of small values due to removing many large values, but it does not change the overall distribution (Figure 2b and 2d). A sensitivity analysis was performed, showing that 50% is a reasonable threshold to balance removal of contamination with keeping reasonable data (not shown).

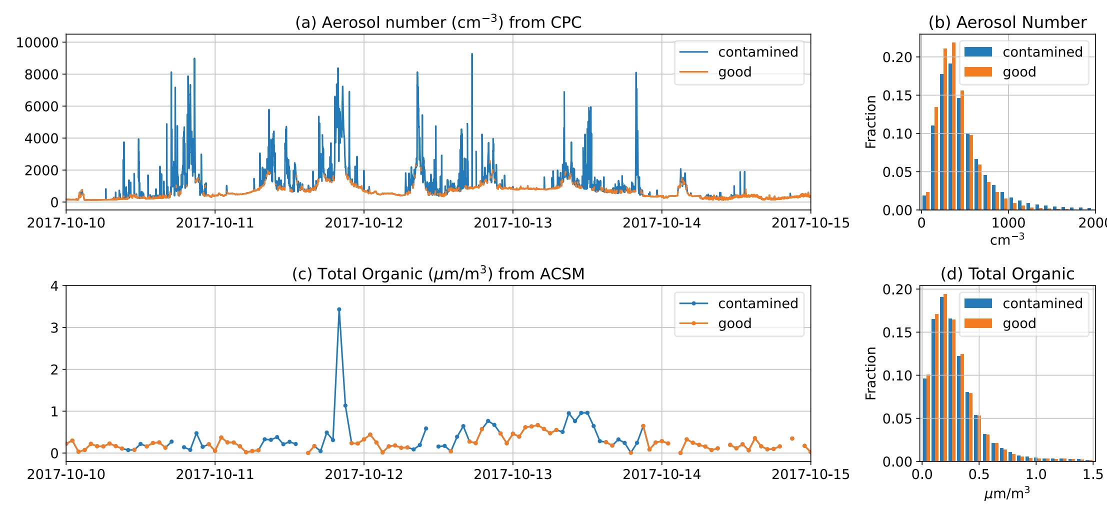

Figure 2: (a) CPC-measured CN from 10 to 15 October 2017 (1-minute resolution) with local contamination flagged by Gallo et al. (2020). (b) histogram of CPC-measured CN for all data from 2016-2018. (c) ACSM measured total organic matter from 10 to 15 October 2017 (1-hour resolution). Hours with more than half or the hour flagged in 1-minute CPC

data are masked as contaminated. (d) histogram of ACSM-measured total organic matter for all data from 2016-2018.

3. Verification of cloud retrievals with in-situ measurements

Cloud microphysical properties such as droplet number concentration (N_d) and effective radius (R_{eff}) are important variables that connect clouds to other aspects in the climate system such as aerosols and radiation. Except in field campaigns where in-situ aircraft measurements are available, remote sensing retrieval algorithms are usually needed to derive these quantities. Several cloud retrieval products from ground and satellite measurements with different algorithms are used in ESMAC Diags v2. This section compares these cloud retrievals with in-situ aircraft measurements to assess retrieval limitation, uncertainty, and utility. N_d and R_{eff} from aircraft measurements taken during HI-SCALE and ACE-ENA field campaigns are calculated from merged cloud droplet number size distributions (mergedSD) from three different cloud probes with different size ranges. The mergedSD covers the size range from 1.5 µm to 9075 µm, covering the entire E3SM cloud droplet size distribution range and extending to rain droplet size range (> 100 µm). For field campaigns used in this study, the aircraft only flied through non-precipitating or drizzling clouds, in which the airborne measurements usually measure rain droplet number 3 to 5 orders of magnitude smaller than cloud droplet number. Therefore, the inclusion of rain droplet size range has ignorable impact on the aircraft-estimated N_d and R_{eff}.

Table 3 lists R_{eff} and N_d retrieval products used in ESMAC Diags v2. We retrieved Nd_sat with input data from VISST products using the algorithms described in Bennartz (2007), but assuming a ratio of the drop volume mean radius to R_{eff} (commonly referred to as k) of 0.74 and a cloud adiabaticity of 80% (Varble et al., 2023). Other datasets are all available as released products. All retrievals assume a horizontally homogeneous single-layer liquid phase cloud with constant N_d throughout the cloud layer. However, retrieval algorithms are usually run for all conditions whenever they return valid values. When assumptions are not satisfied, retrieved properties may contain large errors and likely alter statistics such as increasing the occurrence frequency of small N_d as will be shown next.

Table 3: Cloud droplet effective radius R_{eff} and number concentration N_d retrievals

Variable	Dataset	Platform	Campaign/site	Retrieved from	Reference
R_{eff}	MFRSRCLDOD	Ground	HI-SCALE, ACE-ENA, SGP, ENA	SW diffuse flux, LWP	(Min and Harrison, 1996; Turner et al., 2021)
	VISST	Satellite	HI-SCALE, ACE-ENA, MAGIC, MARCUS, SGP, ENA	Brightness temperature	(Minnis et al., 2011)
	Wu_etal	Ground	ACE-ENA, MAGIC, ENA	Radar reflectivity, LWP	(Wu et al., 2020)
N_d	Ndrop	Ground	HI-SCALE, ACE-ENA, SGP, ENA	LWP, COD, cloud height	(Riihimaki et al., 2021; Lim et al., 2016)
	Nd_sat (calculated from VISST)	Satellite	HI-SCALE, ACE-ENA, MAGIC, MARCUS, SGP, ENA	LWP, COD, CTT	(Bennartz, 2007)

	Wu_etal	Ground	ACE-ENA, MAGIC, ENA	Radar reflectivity, LWP	(Wu et al., 2020)

MFRSRCLDOD: Cloud Optical Properties from the MultiFilter Shadowband Radiometer (MFRSR)
SW: shortwave
COD: cloud optical depth
CTT: cloud top temperature

Figures 3 shows the occurrence fraction histograms of N_d retrievals with aircraft measurements for HI-SCALE and ACE-ENA field campaigns, with the comparison of original temporal resolution versus 30-minute mean, and the use of all available samples and samples that are filtered as overcast (cloud fraction > 90%) low-level (cloud top height < 4 km) clouds. Figure 4 shows similar plots but for R_{eff}. We also selected two cases with single-layer boundary layer stratus or stratocumulus clouds and plotted their timeseries of original-resolution and 30-min averaged R_{eff} and N_d in Figure S1. The high-frequency aircraft measurements and MFRSR/Ndrop retrievals exhibit much larger variability than coarse-frequency retrievals of Wu_etal and VISST. They frequently sample cloud edges or cloud top/base (for aircraft), where N_d is typically less than further into the cloud. This causes large occurrence fractions in the lowest few bins in the N_d histograms (Figure 3a and 3d). The 30-min VISST products also show large occurrence fraction in the lowest N_d bin for HI-SCALE (Figure 3a), likely due to high frequency of partial cloudy condition over continental U.S. Filtering conditions to only include overcast low-level clouds (Figure 3b, e) and averaging into a coarser resolution (Figure 3c, f) both contribute to the reduction of occurrence fraction in small-N_d bins, and make the measurements from different instruments more comparable.

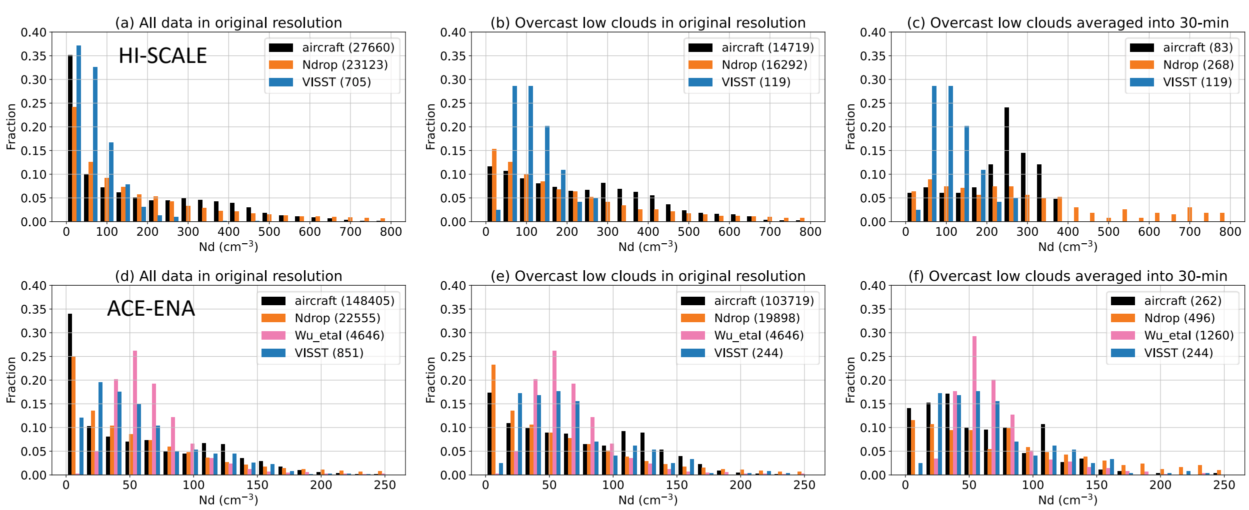

Figure 3: Histogram of N_d from different measurements/retrievals in (top) HI-SCALE and (bottom) ACE-ENA field campaigns, with total sample numbers in the parentheses. (a) and (d) use data samples in their original resolution (1 s for aircraft measurements, 20 s for Ndrop data, 5 min for Wu_etal data, and 30 min for VISST data). (b) and (e) include only overcast low-cloud situations. For aircraft data, this means N_d is > 1 cm^{-3} for 5 s before and after the sampling time; for Ndrop and VISST data, it means cloud fraction > 90% and cloud top height < 4km. (c) and (f) include only overcast low-cloud situations, and

average into 30-min resolution. For all the plots, VISST data with solar zenith angle > 65° are removed to avoid artifact from sunlight.

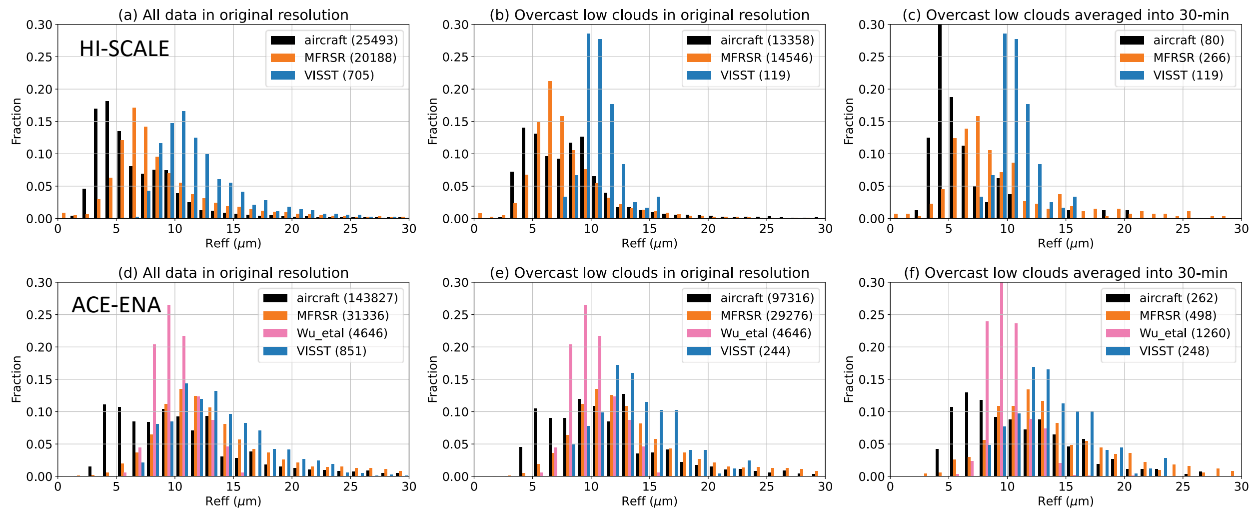

Figure 4: similar as in Figure 3 but for R_{eff}.

Overall, the remote sensing retrievals and aircraft measurements produce reasonable ranges of N_d and R_{eff}. Marine clouds (ACE-ENA) have smaller N_d (Figure 3) and larger R_{eff} (Figure 4) than continental clouds (HI-SCALE). Different retrievals are more consistent with each other for marine clouds than continental clouds. Even after rescaling to the same temporal resolution, aircraft and Ndrop data exhibit broader N_d distributions than satellite retrieval, likely due to their high sampling frequency that may capture more extreme conditions with very high or low N_d. Moreover, the assumption of a fixed adiabaticity (0.8) in satellite retrieval will also narrow N_d distribution. For R_{eff}, we do not expect different datasets to be perfectly agree with each other, as cloud droplet size grows with height in the cloud. All remote sensing retrievals have larger R_{eff} values than aircraft measurements, potentially because remote sensors weight more towards the upper cloud where droplet size and liquid water content (LWC) are larger. Wu_etal retrieves vertical profiles of R_{eff}, and a median value of the R_{eff} profile is used to represent the entire cloud. This makes Wu_etal retrieval weight less toward large droplets thus its R_{eff} is less than MFRSR and VISST. VISST data have the largest R_{eff} values, likely because satellite retrievals reflect conditions at the cloud top. Given the spread in retrieved cloud properties, the limitations and uncertainties of cloud microphysics retrievals clearly need to be considered when they are used to evaluate model performances.

4. Structure of diagnostics package

Figure 5 shows the directory structure of ESMAC Diags v2. It is substantially changed from ESMAC Diags v1 (Tang et al., 2022a). First, we save all data separately as *raw_data,* which stores all input datasets collected from field campaigns, and *prep_data*, which stores preprocessed data with standardized time resolution and quality controls as described in Section 2. The structure is still designed to be flexible for future extension with additional measurements and/or functionality. Second, the diagnostics functions now give users more freedom to modify analyses, such as selecting different time periods, performing additional data filtering or treatments, and examining ACI relationships in specified variable combinations (for scatter plots, joint histograms or heatmaps). We provide a set of example scripts to assist users design their own diagnostics based on their needs. We also provide the source code of data preparation for observations and model output, and a detailed instruction on how to run the code. Users can revise the code to process their own observational data or model output. All the information is available in the ESMAC Diags github repository.

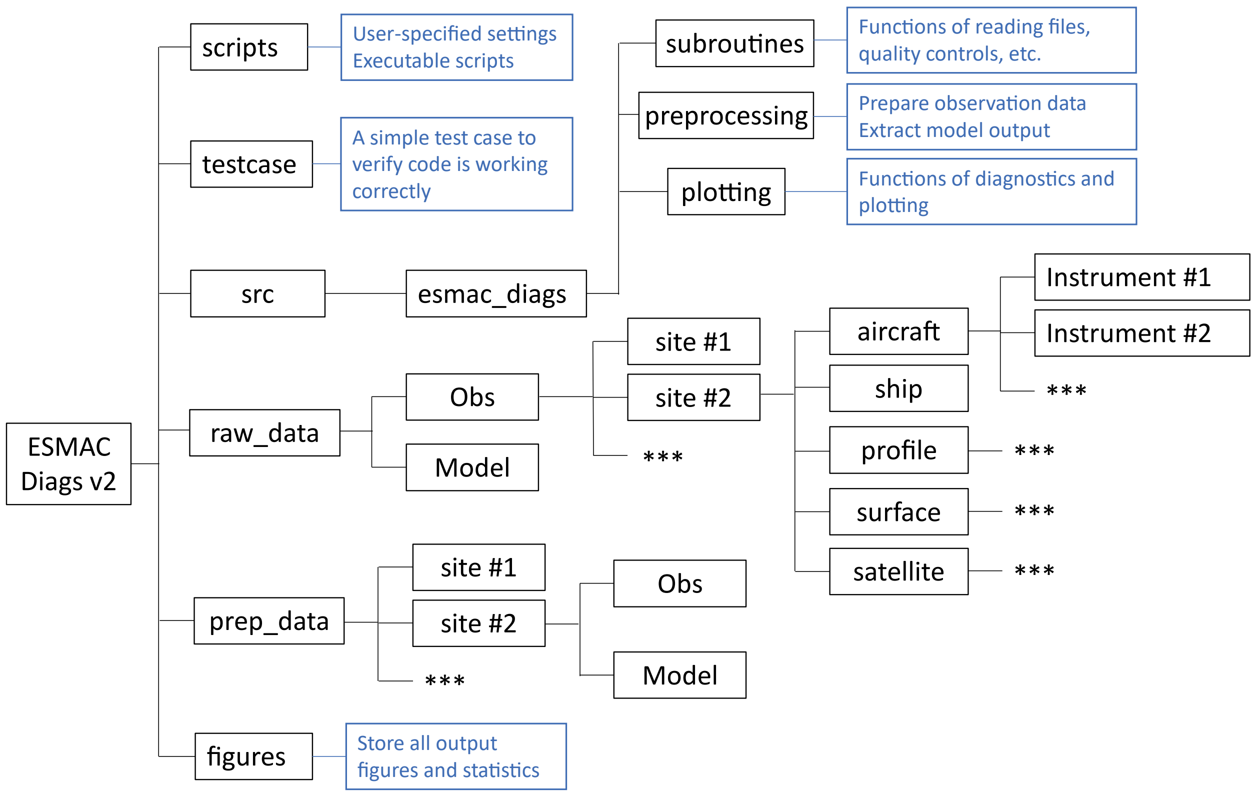

Figure 5: Directory structure of ESMAC Diags v2. Blue boxes describe the functions of the directory. Asterisks represent boxes that follow the same format as those shown in parallel.

ESMAC Diags v1 included diagnostics of aerosol mean statistics (mean, bias, RMSE, correlation), timeseries, diurnal cycle, vertical profiles, mean particle number size distribution, percentiles by height/latitude, and pie/bar charts (Tang et al., 2022a). ESMAC Diags v2 now includes the following new diagnostics that include cloud variables:

- 5^{th}, 25^{th}, 50^{th}, 75^{th} and 95^{th} percentiles,
- Seasonal cycle at SGP and ENA,
- Histograms for individual variables,
- Scatter plots,
- Joint histograms of two variables, and
- Heatmaps of three variables (mean of one variable binned by two other variables).

The inclusion of two-variable scatter plots, joint histograms, and three-variable heatmaps provides the functionality to study ACI-related relationships. We present a few examples in the next section to demonstrate these new diagnostics.

5. Diagnostics Examples

In this section, we show some examples of diagnostics applied to E3SM version 2 (E3SMv2) (Golaz et al., 2022). Compared to the aerosol and cloud parameterizations in E3SMv1 (Rasch et al., 2019; Golaz et al., 2019), E3SMv2 updated the treatments on dust particles, incorporated recalibration of parameters (Ma et al., 2022), changed the call order and refactored the code of the Cloud Layers Unified By Binormals (CLUBB) parameterization, and retuned some parameters (Golaz et al., 2022). We constrain the model simulations by nudging the horizontal winds towards the 3-hourly Modern-Era Retrospective analysis for Research and Applications, Version 2 (MERRA-2, Gelaro et al., 2017) with a nudging time scale of 6 hour. Previous studies have shown that with nudging, E3SM can well simulate the large-scale circulations in reanalyses (Sun et al., 2019; Zhang et al., 2022). The model was run for individual field campaigns (Table 1) and from 2010 to 2020 for long-term diagnostics at SGP and ENA sites, with hourly model output saved over the field campaign regions for detail evaluation. As described in Section 2, all diagnostics for ground and ship campaigns are in 1-hour resolution while diagnostics for aircraft campaigns are in 1-minute resolution. For aerosol and cloud variables, model raw output variables (not from instrument simulators) are used in this paper to reveal the intrinsic ACI relationships in E3SM. However, as can be seen later in this section, instrument simulators can be better used in some diagnostics to ensure more consistent comparison. Users may choose whether or not to use simulators in their diagnostics depending on their purpose.

5.1. Single-variable diagnostics

Figures 6 and 7 show mean and percentile values of aerosol and cloud properties measured from field campaigns in the four geographical regions: CUS, ENA, NEP and SO. Figure 6 is for aircraft platforms and Figure 7 is for ground or ship platforms with satellite data included when available. Note that the aircraft and ground/ship campaigns may cover different time periods (Table 1), thus some differences seen between aircraft and ship measurements may be caused by seasonal variation. As cloud microphysical properties are usually retrieved with assumptions (Section 3), for ground/ship/satellite data, we only focus on overcast low-level liquid cloud condition here (cloud fraction > 90%, cloud top height < 4 km and ice water path < 0.01 mm). E3SM does not output cloud top height, which is derived using a weighting integration method as described in Varble et al. (2023).

From both aircraft and ground/ship data, HI-SCALE has much larger aerosol and cloud droplet number concentrations with smaller droplet sizes compared to other campaigns, which is expected for a continental environment compared to a marine environment. The cloud optical depth is also greater for HI-SCALE than other campaigns, which is driven by smaller droplet sizes rather than LWP differences. Satellite retrievals generally produce smaller N_d, LWP, and cloud optical depth with greater R_{eff} than surface retrievals. As discussed in Section 3, retrieval uncertainties need to be kept in mind when these retrieved microphysical properties are used to evaluate models.

E3SMv2 overestimates CN (> 10 nm) over CUS, ENA and NEP. Larger particle concentration (CN > 100 nm) is generally underestimated over CUS and overestimated over ENA and NEP. Over SO, E3SMv2 produces fewer small aerosol particles (CN > 10 nm) and about the same number of large aerosol particles (CN > 100 nm) compared to the observations. These results are confirmed by both aircraft and ground/ship campaigns, except for the HI-SCALE aircraft campaign where small particles from local emissions were occasionally observed but unable to be simulated. These results are consistent with our previous diagnostics for E3SMv1 (Tang et al., 2022a). E3SMv2 also underestimates N_d over CUS and SO, which corresponds with the underestimation of accumulation mode (> 100 nm) CN over CUS but underestimation of Aitken mode (> 10 nm) CN over SO. It is possible that over very clean regions such as SO, small particles are more important in cloud formation than over continental regions such as CUS. Simulated LWP (LWC) is generally consistent with satellite (aircraft) measurements, but smaller than ground/ship measurements, which may be partly caused by rain contamination of ground/ship retrievals. R_{eff} evaluation is less certain given large discrepancies between satellite and ground retrievals.

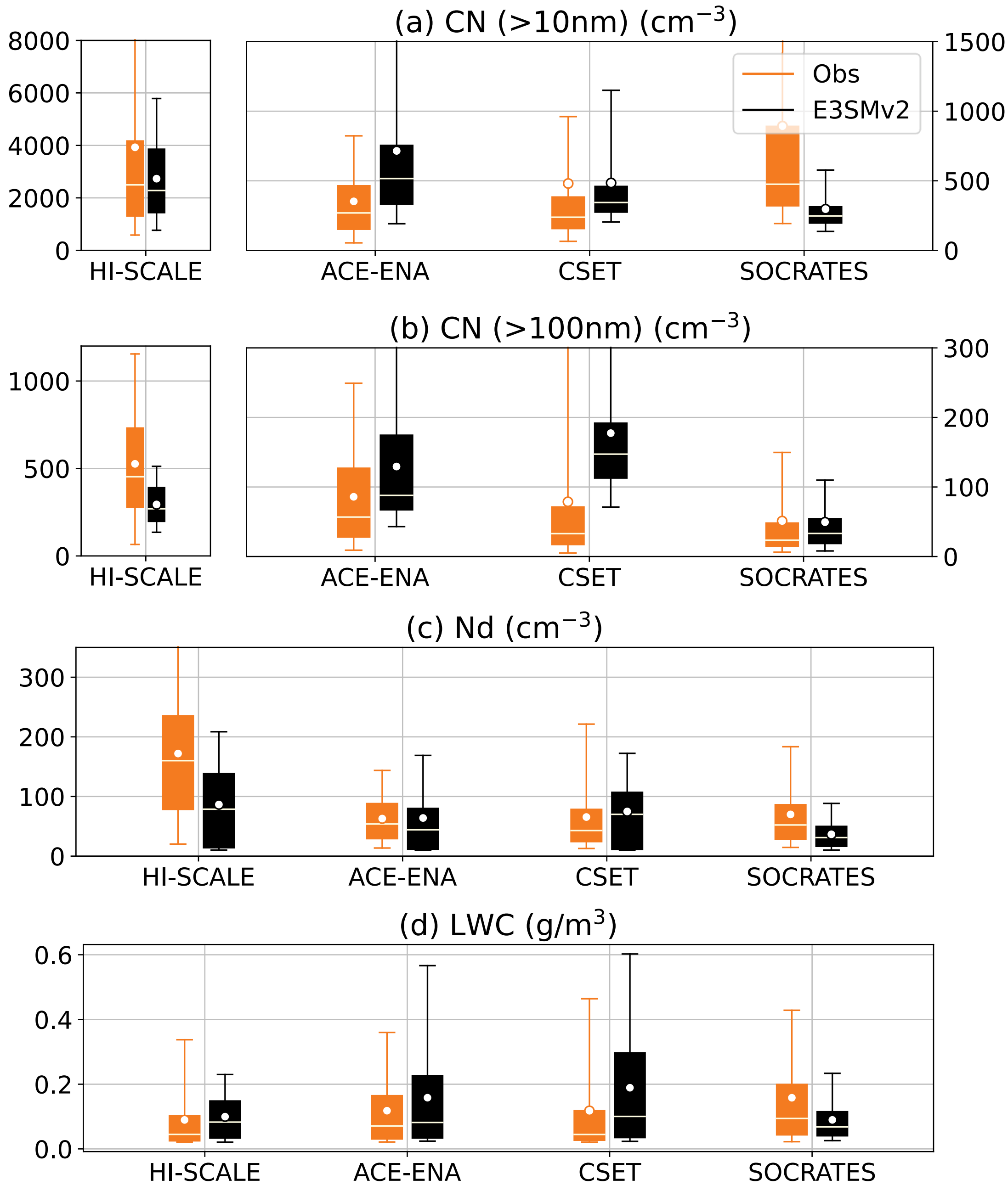

Figure 6: Box-whisker plots of (a) CN for size > 10 nm, (b) CN for size > 100 nm, (c) in-cloud N_d, (d) LWC for all data from aircraft field campaigns at CUS, ENA, NEP and SO regions from left to right. Boxes denote 25th and 75th percentiles, whiskers denote 5th and 95th percentiles, the white horizontal line represents median values, and the white dot represents mean values. For aerosol number concentrations, the y axes for HI-SCALE are separated from other field campaigns for better visualization. The top whiskers that are out of the y-axis range are: (a) HI-SCALE obs: 13681. ACE-ENA E3SMv2: 2061. SOCRATES obs: 2745. (b): ACE-ENA E3SMv2: 304. CSET obs: 305. CSET E3SMv2: 400. (c): HI-SCALE obs: 397.

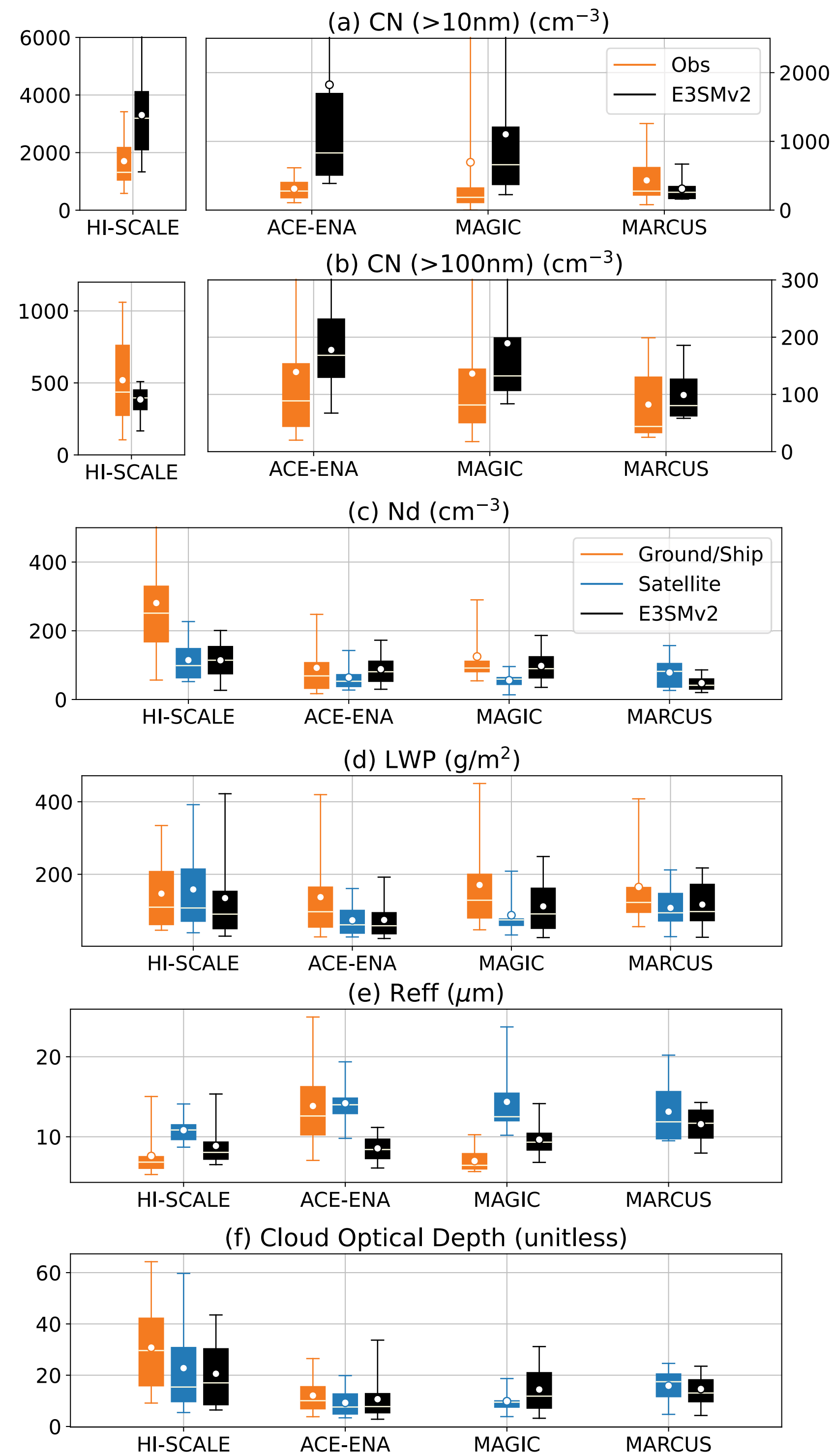

Figure 7: Box-whisker plots of (a) CN for size > 10 nm, (b) CN for size > 100 nm, (c) layer-mean N_d, (d) LWP, (e) R_{eff}, (f) cloud optical depth for overcast low-level liquid cloud conditions (cloud top height < 4 km, cloud fraction > 90% and ice water path < 0.01 mm) in ground and ship field campaigns at CUS, ENA, NEP and SO regions from left to right. Boxes denote 25th and 75th percentiles, whiskers denote 5th and 95th percentiles, the

white horizontal line represents median values, and the white dot represents mean values. For aerosol number concentrations, the y axes for HI-SCALE are separated from other field campaigns for better visualization. The top whiskers that are out of the y-axis range are: (a) HI-SCALE E3SMv2: 6102. ACE-ENA E3SMv2: 7575. MAGIC obs: 3330. MAGIC E3SMv2: 3771. (b): ACE-ENA obs: 304.7. ACE-ENA E3SMv2: 328.3. MAGIC obs: 377.7. MAGIC E3SMv2: 577.8. (c): HI-SCALE obs: 670.9.

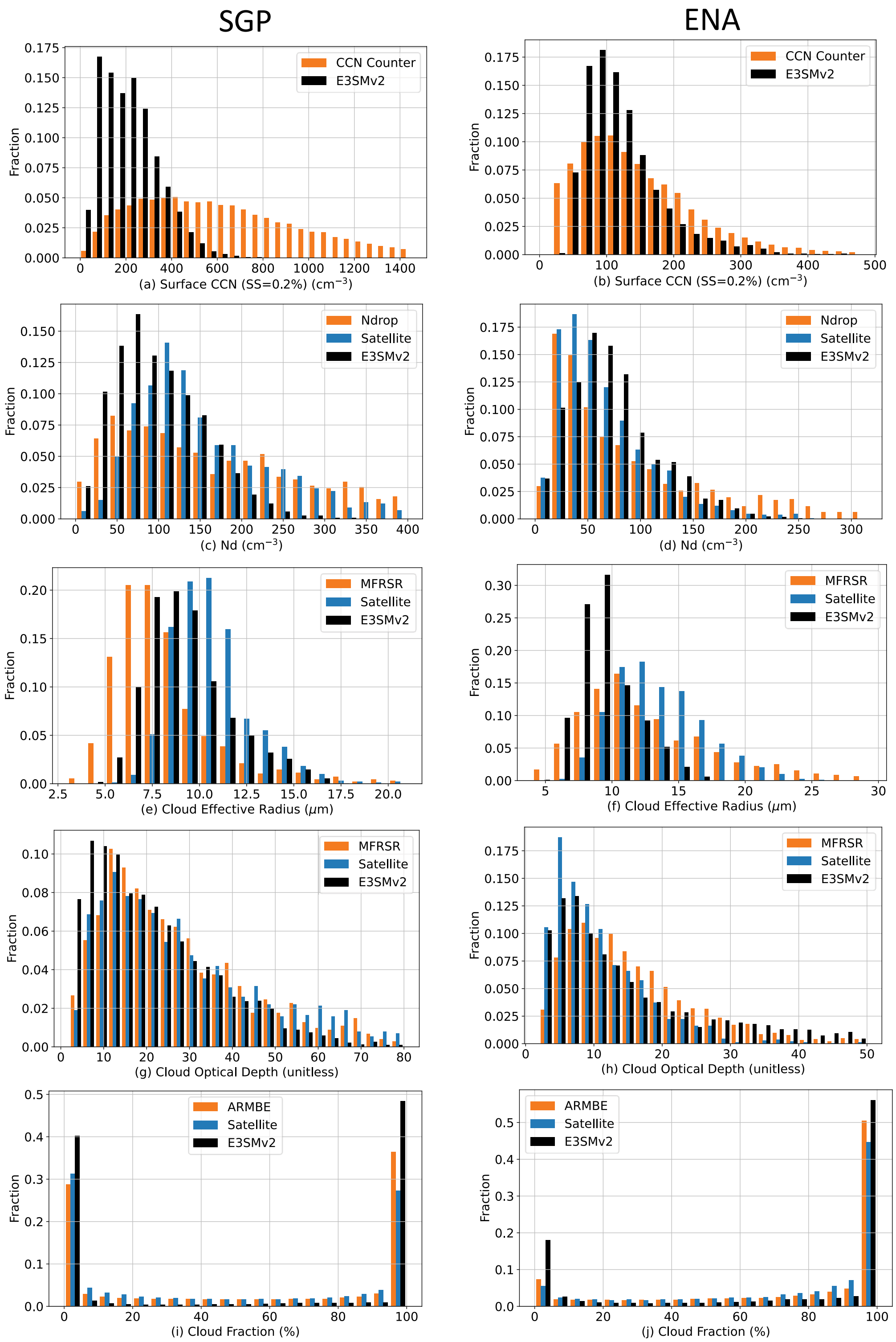

Figure 8: histogram of (from top to bottom) surface CCN number concentration, layer-mean N_d, R_{eff}, cloud optical depth and total cloud fraction at (left) SGP from 2011 to 2020 and (right) ENA from 2016 to 2018. Surface CCN and total cloud fraction are using all-condition samples while N_d, R_{eff}, cloud optical depth data are filtered for overcast

low-level liquid clouds (cloud top height < 4 km, cloud fraction > 90%, ice water path < 0.01 mm).

Figure 8 shows histograms of surface CCN number concentration in 0.2% supersaturation, cloud layer mean N_d, R_{eff}, cloud optical depth and total cloud fraction for long-term diagnostics at SGP (year 2011-2020) and ENA (year 2016-2018) sites. E3SMv2 fails to reproduce the long tail of large values in CCN and N_d, especially over SGP. This is consistent with the underestimation of CN (> 100 nm) during the HI-SCALE field campaign shown in Figures 6 and 7. Compared with ground retrievals, E3SMv2 R_{eff} is larger at SGP but smaller at ENA. However, satellite-retrieved R_{eff} has larger values than E3SMv2 at SGP. As discussed before, discrepancies between satellite and ground retrievals can be substantial for some locations and variables, and considering both in evaluating model performance gives a sense for how uncertain comparisons are. E3SMv2 generally captures the histograms of cloud optical depth and total cloud fraction, although it underestimates the frequency of partial-cloudy conditions and overestimates the frequency of clear-sky and overcast conditions.

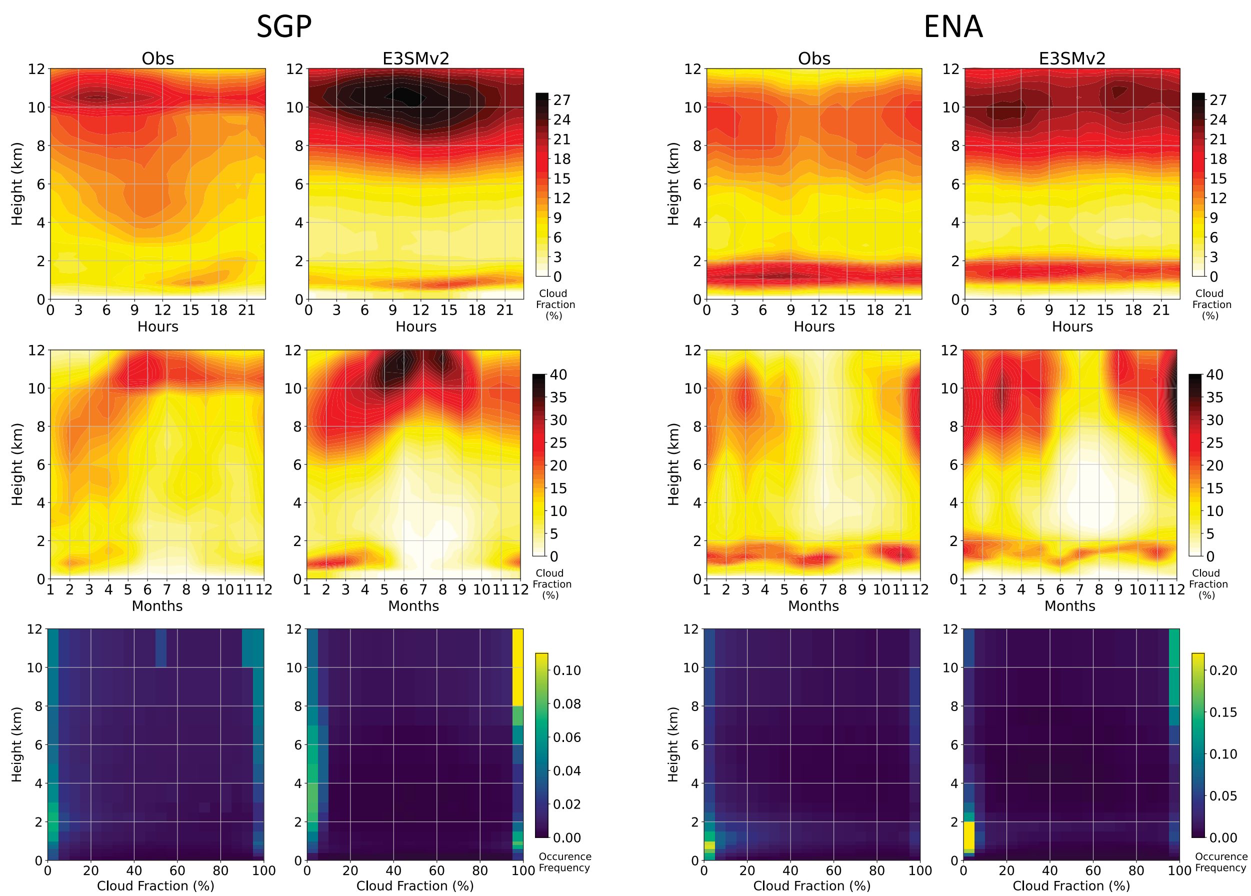

Figure 9: (top) Diurnal cycle, (middle) seasonal cycle, and (bottom) occurrence frequency of vertical cloud fraction at (left) SGP from 2011 to 2020 and (right) ENA from 2016 to 2018.

Figure 9 shows the long-term diagnostics of mean diurnal cycles, seasonal cycles and histograms of cloud fraction by height at SGP and ENA sites. Overall, the mean fraction of high clouds looks overestimated in E3SMv2. Similar results has been reported in many previous studies in the Community Earth System Model (CESM)-E3SM model family (e.g., Song et al., 2012; Cheng and Xu, 2013; Xu and Cheng, 2013b, a; Tang et al., 2016; Zhang et al., 2020). However, this is not an apple-to-apple comparison, as cloud fraction in ESMs includes clouds that are optically very thin that cannot be detected by satellite passive sensors or cloud radars. The comparison of high cloud fraction from simulators with the corresponding satellite observations showed that E3SM slightly underestimates high clouds over most tropical deep convection regions (Zhang et al., 2019; Xie et al., 2018; Rasch et al., 2019). Unfortunately, ground-based radar simulator of cloud vertical profiles is not available in the current model, which prevents a direct apple-to-apple comparison. Thus, caution should be taken when comparing magnitude of cloud fraction from direct model output and radar measurements. Here we focus on the temporal variabilities (diurnal and seasonal cycles) and the occurrence frequency distribution of cloud fraction, which are less relevant to the detection threshold of cloud radars.

At SGP, observations show formation of low clouds in the afternoon and in late winter through springtime. High clouds peak overnight into the early morning and in the spring to summer, corresponding to nocturnal deep convective systems common over SGP (Tang et al., 2022b; Tang et al., 2021; Jiang et al., 2006). These features are reasonably well represented in E3SMv2, although low-level cloud deepening in the afternoon is not well predicted, and high-level clouds peak in the late rather than early morning. At ENA, marine stratus or stratocumulus clouds occur in any month and at any time of the day, but with less frequency in late summer and in afternoon. High clouds are more frequent in winter months than in summer months and occur throughout the diurnal cycle with a slight mid-day minimum. These features are well captured by E3SMv2. At both sites, high clouds usually occur with high fraction (> 95%) while low clouds are more likely associated with small fraction (< 5%) (bottom row). At SGP, high occurrence of low cloud fraction extends vertically up to the tropopause, representing frequently occurring deep convection. At ENA, low clouds have less vertical extension but are more likely to expand to greater fraction. E3SMv2 reproduces these cloud features in occurrence frequency.

5.2. Multi-variable relationships related to ACI

The effective radiative forcing due to ACI processes are complex, nonlinear, and highly uncertain despite their significant impact on climate. ACI studies are usually conducted by examining relationships between aerosols, clouds, and radiation variables that are known to interact with one another. Given so many variable combinations related to ACI, ESMAC Diags v2 provides a framework for users to examine relationships between the variables they choose with joint histograms, scatter plots and heatmaps. Here we show a few examples to assess relationships between CCN, N_d, LWP, and top of atmosphere (TOA) albedo. ESMAC Diags v2 calculate layer-mean N_d from three sources: integrated vertically from native model output, retrieved using Ndrop algorithm and using Nd_sat algorithm, as shown in Table 3. In this study we only show the ACI diagnostics using native model output, as it reveals the “true” ACI relations in the model. Users can choose to use the retrieved N_d in their studies for their purposes.

The dependence of TOA albedo on CCN number concentration for stratiform warm clouds can be decomposed (e.g., following Quaas et al. (2008)) as:

$$\frac{dA}{dlnCCN} = \left(\frac{\partial A}{\partial lnN_d} + \frac{\partial A}{\partial lnLWP}\frac{dlnLWP}{dlnN_d}\right)\frac{dlnN_d}{dlnCCN} \quad (1)$$

which allows isolation of "Twomey effect" ($\frac{\partial A}{\partial lnN_d}$) ($\frac{dlnN_d}{dlnCCN}$) and "LWP adjustment" ($\frac{dlnLWP}{dlnN_d}$) associated with specific ACI processes. Here we use joint histograms and heatmaps to evaluate each component, $\frac{dlnN_d}{dlnCCN}$, $\frac{dlnLWP}{dlnN_d}$, $\frac{\partial A}{\partial lnN_d}$ and $\frac{\partial A}{\partial lnLWP}$ based on long-term ground and satellite measurements at SGP (2011-2020) and ENA (2016-2018) sites. The analysis in this section (except Figure 11) is limited to overcast (cloud fraction > 90%), low-level (cloud top height < 4 km) liquid (ice water path < 0.01 mm) clouds. Since there is no direct measurement of cloud base CCN concentration from remote sensors, surface CCN concentration is used in this study and only clouds that are most likely to be affected by surface conditions are examined. These clouds are identified as having cloud base potential temperature minus surface potential temperature smaller than 2 K. For satellite measurements, samples with solar zenith angle greater than 65° are removed to avoid N_d retrieval biases (Grosvenor et al., 2018). The sample number of (ground, satellite, E3SM) for overcast low-level liquid clouds are (1766, 1217, 6369) at SGP and (3450, 1345, 2884) at ENA, respectively. To increase sample size for more robust statistics, satellite retrievals and E3SM outputs over a 5°×5° domain centered on SGP and ENA sites are included. This increases the sample number to (1766, 71942, 15231) at SGP and (3450, 104260, 28184) at ENA. Analyses of all-sky conditions and overcast low-level liquid clouds for a single grid point over each site are shown in Figures S2-S7 in the supplementary material. Increasing sample domain for satellite and E3SM data does not change the overall statistics shown here.

The change of N_d in response to a change of surface CCN number concentration ($\frac{dlnN_d}{dlnCCN}$) is heavily influenced by processes such as aerosol activation. Figure 10 shows the joint probability density function (PDF)of N_d and surface CCN number concentration at 0.1% supersaturation normalized within each CCN bin. Ground and satellite observations show similar linear fit of $lnN_d - lnCCN$ relation, although ground-based plots have much smaller sample number. E3SMv2 shows more sensitive N_d – CCN relationships than observations at both SGP and ENA sites, with the relationship tighter at ENA and more scattered at SGP. As a cross validation, Figure 11 shows the N_d – CCN relationships from short-term aircraft campaign during HI-SCALE and ACE-ENA. The comparison with in-situ aircraft measurements confirms that E3SMv2 has more sensitive N_d to CCN relationship than observations. These results indicate that aerosol activation in E3SMv2 may be too weak in low CCN conditions and too strong in high CCN conditions, which may be related to the differences in simulated and observed updraft velocity and supersaturation. Note that E3SMv2 produces a significant number of small N_d (< 20 cm^{-3}) samples (Figure 11). This feature is reported in Golaz et al. (2022) and is partially removed by setting a minimum threshold of N_d = 10 cm^{-3}. However, as seen in Figure 11, there are still a large number of N_d between 10 and 20 cm^{-3}. Further investigation is underway to diagnose the causes of the abundant low-N_d values. The diagnostics shown here indicate that a more physical method should be applied to improve the simulated N_d.

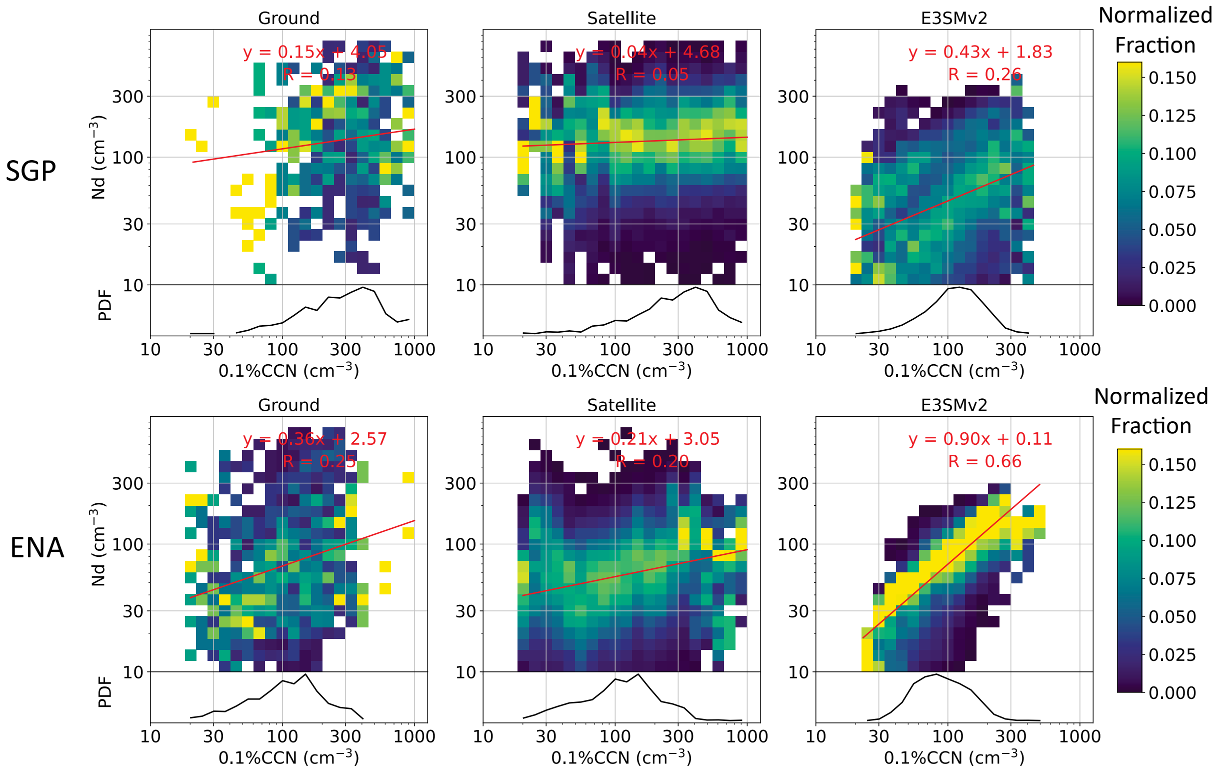

Figure 10: Joint histogram of layer-mean N_d versus surface CCN number concentration at 0.1% supersaturation, normalized within each CCN number concentration bin (PDF of CCN shown in the bottom of each panel). Samples are constrained to likely surface-coupled, overcast low-level liquid clouds (cloud top height < 4 km, cloud fraction > 90%, ice water path < 0.01 mm and potential temperature difference between cloud base and surface < 2 K). Available samples within a 5°×5° region centered on SGP (top) and ENA (bottom) for satellite and E3SMv2 datasets are included. Linear fits and R values are shown in red.

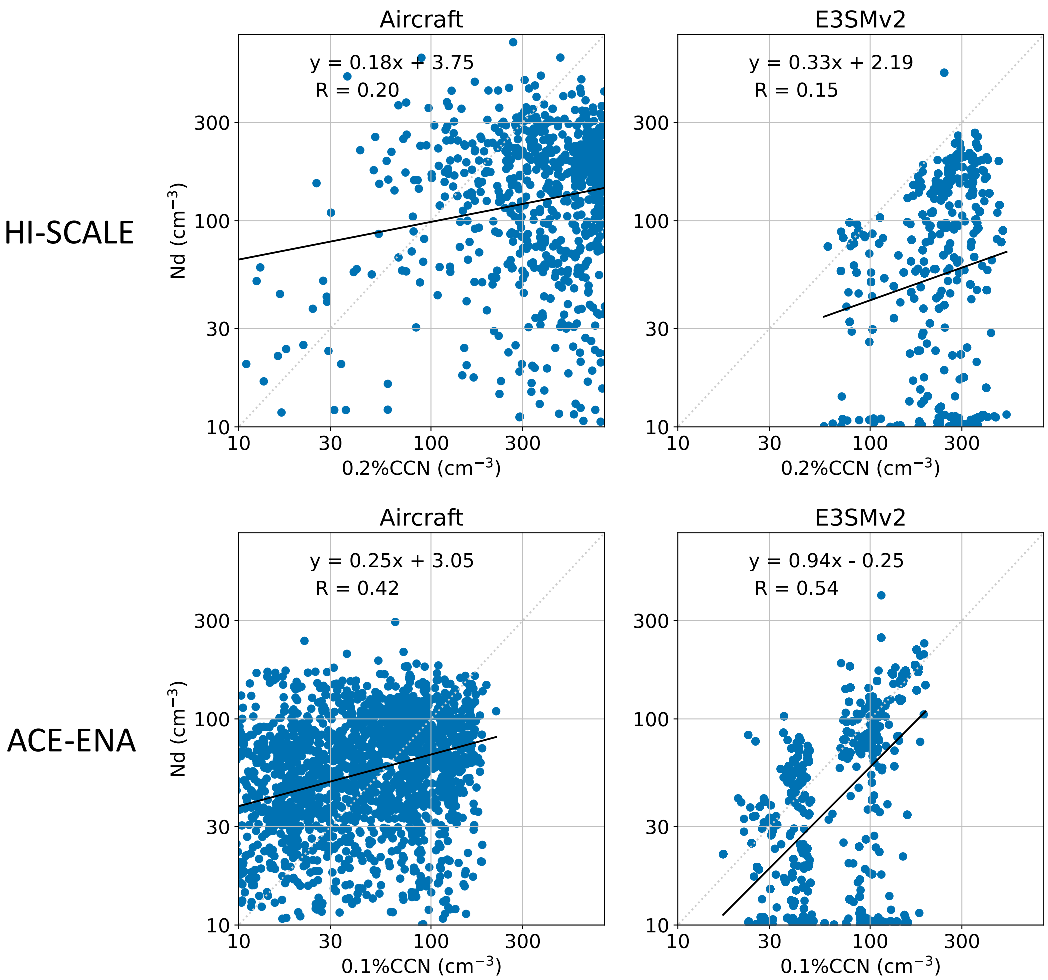

Figure 11: Scatter plots for N_d versus CCN along the flight tracks from (top) HI-SCALE and (bottom) ACE-ENA campaigns. Note that CCN number concentration measurements are taken under ~0.2% supersaturation for HI-SCALE and under ~0.1% supersaturation for ACE-ENA. Linear fits and R values are shown in each panel. R = 0.34 (SGP) and 0.74 (ENA) for E3SMv2 if a minimum N_d = 20 cm^{-3} is applied.

The term $\frac{dlnLWP}{dlnN_d}$ is commonly interpreted as the response of LWP to a perturbation in N_d tied to suppression of precipitation (increase LWP) or enhancement of evaporation (decrease LWP) (e.g., Glassmeier et al., 2019). Gryspeerdt et al. (2019) show that the satellite retrieved LWP over ocean increases with N_d when $N_d < \sim 30\ cm^{-3}$ and decreases when $N_d > \sim 30\ cm^{-3}$. This relation is also seen in satellite retrievals at ENA (Figure 12) when using a higher threshold $N_d = 50\ cm^{-3}$ to perform linear fits (black dashed lines). The linear fit is insignificant for $N_d < 50\ cm^{-3}$ in surface retrievals at both sites, partly due to small sample number, and also potentially related to drizzle contamination of LWP. The slope of the LWP – N_d relation in satellite retrievals at SGP is positive for both N_d ranges. This is opposed to the slope from the ground retrievals and satellite retrievals at ENA. This result reveals a few difficulties on LWP susceptibility studies based on observations. First, limitations of instruments and their platforms (from space or from ground) employed in these observations as well as assumptions and simplifications in their retrieval algorithms, may introduce biases and uncertainties into the retrieved cloud microphysical properties. These biases and uncertainties can be amplified when studying ACI relationships between multiple variables. Second, the robustness of ACI studies is also dependent on geographical locations and cloud types, with environmental dynamic conditions influencing the analytical outcomes. Despite our efforts to constrain meteorology and cloud situations, it is essential to acknowledge the existence of many other factor, such as cloud adiabaticity and solar zenith angle as discussed in Varble et al. (2023)), which can impact cloud susceptibility. Given these limitations and uncertainties, researchers should use caution when using observational data to study ACI relationships. ~~slope shown in the ground retrievals and indicates that retrieval biases may cause opposite results in ACI studies. The reason why satellite retrievals show positive LWP – N_d relation at SGP is subject to further investigation.~~

The E3SMv2 simulated LWP – N_d relation is quite different from satellite retrievals at both sites. At SGP, it generates a positive slope for $N_d < 50\ cm^{-3}$, and a negative slope for $N_d > 50\ cm^{-3}$. At ENA, it shows an opposite relation, with LWP decreases for small N_d and increases for large N_d. The overall LWP susceptibility in E3SMv2 is negative, which is consistent with observations and but differs from most ESMs that produce a positive value (Quaas et al., 2009; Gryspeerdt et al., 2020). However, the observed inverted "V" relation of LWP to Nd is oppositely seen in E3SMv2. We examined a few other oceanic regions with frequent stratus or stratocumulus clouds ~~in E3SMv2~~ and saw similar behavior (not shown). This indicates possible different mechanisms of LWP susceptibility in E3SM than in observations. ~~However, LWP – N_d relation in E3SMv1 performs quite differently, as shown in . The causes of the different LWP – N_d relation behaviors in E3SM are under further investigation. discussed potential physical mechanisms that may affect the different LWP responses to N_d in observation and simulation, such as different atmospheric states in E3SM and observations.~~ Our user-friendly diagnostics package allows these analyses to be routinely performed for the purpose of better understanding critical model behaviors at process- and mechanistic-levels, providing observational constraints to facilitate model development efforts.

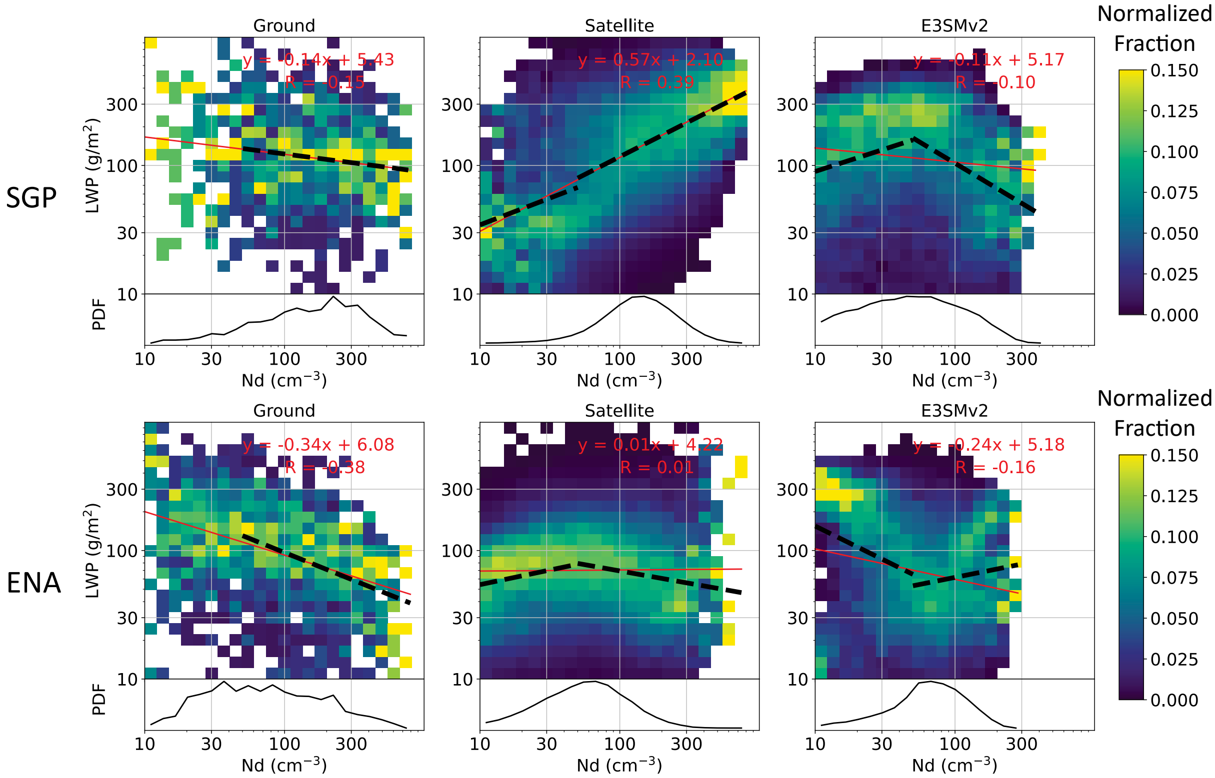

Figure 12: Following Figure 10, but for the N_d bin-normalized joint histogram of LWP versus N_d. Red lines and equations are linear fits for all data samples and black dashed lines are linear fits for $N_d < 50\ cm^{-3}$ and $N_d > 50\ cm^{-3}$ when the fits are statistically significant (p < 0.01).

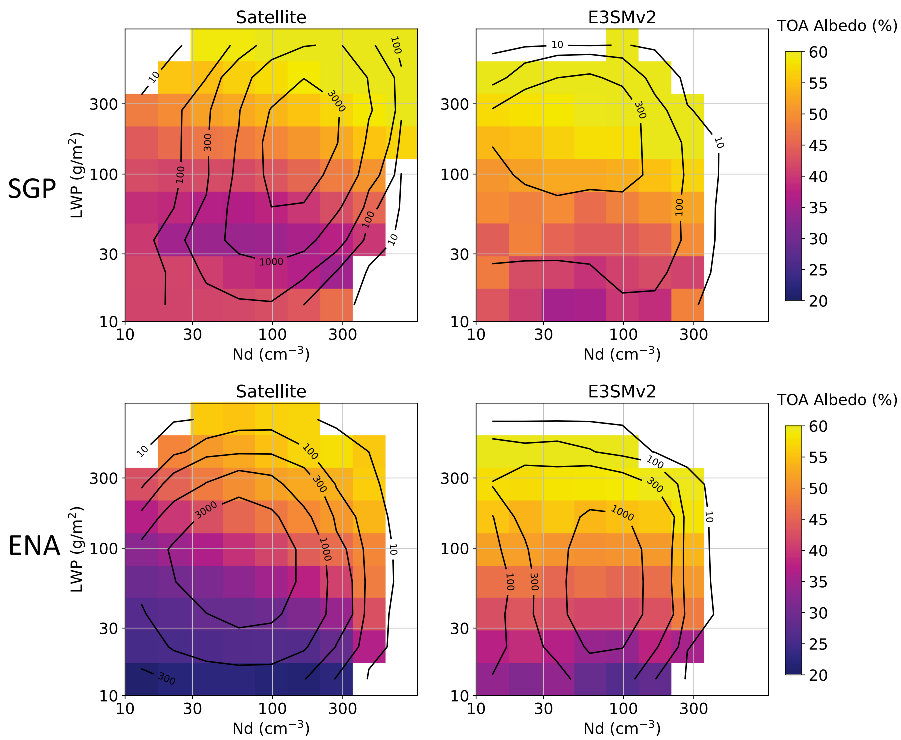

Figure 13: Heatmaps of mean TOA albedo versus LWP and N_d for likely surface-coupled, overcast low-level liquid clouds (cloud top height < 4 km, cloud fraction > 90%, ice water path < 0.01 mm and potential temperature difference between cloud base and surface < 2 K). Data include samples within a 5°×5° region centered on SGP (top) and ENA (bottom). Valid sample number is shown in black contour lines. Grids with valid sample number < 10 are not filled. Ground data is not included, since the TOA albedo is not available.

Figure 13 shows heatmaps of mean TOA albedo with respect to LWP and N_d from which $\frac{\partial A}{\partial lnN_d}$ and $\frac{\partial A}{\partial lnLWP}$ can be derived. At both ENA and SGP, TOA albedo generally increases with increases of LWP and N_d, except at SGP when LWP is small. The increasing albedo in small LWP may be due to retrieval artifact as uncertainty becomes large when LWP is small (e.g., < 20 g/m^2), solar zenith angle is large (e.g., > 55°), or cloud optical depth is small (e.g., <5) (Grosvenor et al., 2018). In most LWP-N_d bins, TOA albedo at SGP is generally higher than at ENA, which is expected for clouds with smaller droplet sizes. Increasing TOA albedo with increases of LWP is also seen in E3SMv2, but the dependence with N_d is weak. This can be impacted by correlation between solar zenith angle and N_d in E3SM simulation, as discussed in Varble et al. (2023). For a given LWP and N_d, TOA albedo is generally higher in E3SMv2 than in satellite observations, indicating that shallow clouds may be too reflective in the model, possibly due to smaller cloud R_{eff} (Figure 8).

The above illustration of single-variable and multi-variable diagnostics present examples to demonstrate the capability of ESMAC Diags v2. More analyses, such as selecting other variables, performing additional data filtering or treatments, and examining ACI relationships with other variable combinations, can be conducted through user-specified settings. A detailed user guide and a collection of example scripts are included in the diagnostics package to assist users design customized diagnostics suited to their specific needs.

5. Summary

We developed the Earth System Model aerosol-cloud diagnostics package (ESMAC Diags) to facilitate routine evaluation of aerosols, clouds and ACI in the U.S. DOE's E3SM model using multiple platforms of observations. As an updated version of ESMAC Diags v1 (Tang et al., 2022a) which mainly focuses on aerosol properties, this paper described ESMAC Diags v2 that focuses on both aerosols, clouds, as well as their interactions. In addition to the short-term field campaigns included in ESMAC Diags v1, long-term diagnostics from two permanent ARM sites (SGP and ENA, each represents continental and maritime conditions, respectively) are now conducted to provide more robust evaluation. The newly added multi-variable joint histograms, scatter plots and heatmaps allow users to examine correlations between variables that are relevant to the study of ACI.

Ground- and ship-based aerosol measurements are frequently impacted by local-scale emissions sources such as those from airport or ship exhaust. These local sources are not resolved by coarse-resolution ESMs, which usually represent an environment averaged within a region of tens to hundreds of kilometers in size. In ESMAC Diags, we used available contamination-removed aerosol data, such as those from Gallo et al. (2020) for ENA, and Humphries (2020) for MARCUS, and applied data filtering for other field campaigns. The observations are harmonized into a uniform data format and temporal resolution that are comparable with ESMs. Aircraft measurements retain higher resolution (currently 1-min) to preserve high spatiotemporal variability, although ESMs have to be downscaled for evaluation with aircraft measurements. This limitation of scale mismatch must be accepted to perform evaluation in current coarse-resolution ESMs. Nevertheless, as ESM grid spacing approaches a few kilometers via regional refinement (Tang et al., 2019) or global convection-permitting configuration (Caldwell et al., 2021), the scale inconsistency between models and observations is reduced. ESMAC Diags can easily adjust the preprocessing output resolution to facilitate the evaluation of high-resolution model output.

Cloud microphysical properties heavily rely on remote sensing measurements to achieve more robust sampling, with imperfect retrieval algorithms needed to estimate these variables. Microphysical retrievals are more uncertain than typical atmospheric state measurements due to the need for many assumptions related to cloud dynamical and physical processes. We have shown (in Section 3) that ground- and satellite-based retrievals of N_d and R_{eff} are overall consistent with each other and with in-situ aircraft measurements, with some systematic differences such as smaller N_d and larger R_{eff} in satellite retrievals. The discrepancies between different retrievals can be larger for individual days (e.g., Figure S1) but can be mitigated to some degrees when considering broader statistics (Figures 3 and 4). The usage of multiple retrieval datasets is critical to understand the robustness of evaluation results, as the spread between different datasets indicates how robust model-observation differences are and guides interpretations of model biases to support model development.

Finally, this paper presents a few examples of how well E3SMv2 simulates aerosols, clouds and ACI. We showed that ESMAC Diags can be used to target further investigation into specific parameterization components. For example, the analysis of N_d – CCN correlation indicates that E3SMv2 may exhibit too weak aerosol activation in low CCN conditions and too strong in high CCN conditions; the analysis of LWP – N_d correlation indicates that either the precipitation suppression and cloud evaporation mechanisms are not well represented, or there are other mechanisms dominating LWP – N_d correlation in E3SMv2. These diagnostic analyses provide insights into areas in aerosols, clouds and ACI that warrant special attention in future model development efforts. As ESMs continuously improve its physical parameterizations, resolution, and numerical schemes, ESMAC Diags offers a valuable tool for systematically evaluating the performance of the newer versions of a model in simulating aerosol, clouds and ACI.

Code availability:

The current version of ESMAC Diags is publicly available through GitHub (https://github.com/eagles-project/ESMAC_diags) under the new BSD license. The exact version (2.1.2) of the code used to produce the results used in this paper is archived on Zenodo (https://doi.org/10.5281/zenodo.7696871). The model simulation used in this paper is version 2.0 (https://doi.org/10.11578/E3SM/dc.20210927.1) of E3SM.

Data availability:

Measurements from the HI-SCALE, ACE-ENA, MAGIC, and MARCUS campaigns as well as the SGP and ENA sites are supported by the DOE Atmospheric Radiation Measurement (ARM) user facility and available at https://adc.arm.gov/discovery/. Measurements from the CSET and SOCRATES campaigns are supported by National Science Foundation (NSF) and obtained from NCAR Earth Observing Laboratory at https://data.eol.ucar.edu/master_lists/generated/cset/ and https://data.eol.ucar.edu/master_lists/generated/socrates/, respectively. DOI numbers or references of individual datasets are given in Tables S1-S8. All the preprocessed observational and model data used to produce the results used in this paper is archived on Zenodo (https://doi.org/10.5281/zenodo.7478657).

Author contribution:

ST, JDF and PM designed the diagnostics package; ST and ACV wrote the code and performed the analysis; PW, XD, FM and MP processed the field campaign datasets and provided discussions on the data quality issues; KZ contributed to the model simulation; JCH contributed to the package design and setup; ST wrote the original manuscript; all authors reviewed and edited the manuscript.

Competing interests:

Po-Lun Ma is a Topical Editor of Geoscientific Model Development. Other authors declare that they have no conflict of interest.

***Acknowledgements**:*

This study was supported by the Enabling Aerosol-cloud interactions at GLobal convection-permitting scalES (EAGLES) project (74358), funded by the U.S. Department of Energy, Office of Science, Office of Biological and Environmental Research, Earth System Model Development (ESMD) program area. We thank the numerous instrument mentors for providing the data. This research used resources of the National Energy Research Scientific Computing Center (NERSC), a U.S. Department of Energy Office of Science User Facility operated under Contract No. DE-AC02-05CH11231, using NERSC awards ALCC-ERCAP0016315, BER-ERCAP0015329, BER-ERCAP0018473, and BER-ERCAP0020990. Pacific Northwest National Laboratory (PNNL) is operated for DOE by Battelle Memorial Institute under contract DE-AC05-76RL01830.

References:

Albrecht, B., Ghate, V., Mohrmann, J., Wood, R., Zuidema, P., Bretherton, C., Schwartz, C., Eloranta, E., Glienke, S., Donaher, S., Sarkar, M., McGibbon, J., Nugent, A. D., Shaw, R. A., Fugal, J., Minnis, P., Paliknoda, R., Lussier, L., Jensen, J., Vivekanandan, J., Ellis, S., Tsai, P., Rilling, R., Haggerty, J., Campos, T., Stell, M., Reeves, M., Beaton, S., Allison, J., Stossmeister, G., Hall, S., and Schmidt, S.: Cloud System Evolution in the Trades (CSET): Following the Evolution of Boundary Layer Cloud Systems with the NSF–NCAR GV, Bull. Amer. Meteor. Soc., 100, 93-121, 10.1175/bams-d-17-0180.1, 2019.

AMWG Diagnostic Package: https://www.cesm.ucar.edu/working_groups/Atmosphere/amwg-diagnostics-package/, last access: 2 November 2021.

Bennartz, R.: Global assessment of marine boundary layer cloud droplet number concentration from satellite, Journal of Geophysical Research: Atmospheres, 112, 10.1029/2006JD007547, 2007.

Caldwell, P. M., Terai, C. R., Hillman, B., Keen, N. D., Bogenschutz, P., Lin, W., Beydoun, H., Taylor, M., Bertagna, L., Bradley, A. M., Clevenger, T. C., Donahue, A. S., Eldred, C., Foucar, J., Golaz, J.-C., Guba, O., Jacob, R., Johnson, J., Krishna, J., Liu, W., Pressel, K., Salinger, A. G., Singh, B., Steyer, A., Ullrich, P., Wu, D., Yuan, X., Shpund, J., Ma, H.-Y., and Zender, C. S.: Convection-Permitting Simulations With the E3SM Global Atmosphere Model, Journal of Advances in Modeling Earth Systems, 13, e2021MS002544, 10.1029/2021MS002544, 2021.

Cheng, A. and Xu, K.-M.: Evaluating Low-Cloud Simulation from an Upgraded Multiscale Modeling Framework Model. Part III: Tropical and Subtropical Cloud Transitions over the Northern Pacific, J. Climate, 26, 5761-5781, 10.1175/JCLI-D-12-00650.1, 2013.

Choudhury, G. and Tesche, M.: Estimating cloud condensation nuclei concentrations from CALIPSO lidar measurements, Atmos. Meas. Tech., 15, 639-654, 10.5194/amt-15-639-2022, 2022.

E3SM Diagnostics: https://e3sm.org/resources/tools/diagnostic-tools/e3sm-diagnostics/, last access: 2 November 2021.

Eyring, V., Righi, M., Lauer, A., Evaldsson, M., Wenzel, S., Jones, C., Anav, A., Andrews, O., Cionni, I., Davin, E. L., Deser, C., Ehbrecht, C., Friedlingstein, P., Gleckler, P., Gottschaldt, K. D., Hagemann, S., Juckes, M., Kindermann, S., Krasting, J., Kunert, D., Levine, R., Loew, A., Mäkelä, J., Martin, G., Mason, E., Phillips, A. S., Read, S., Rio, C., Roehrig, R., Senftleben, D., Sterl, A., van Ulft, L. H., Walton, J., Wang, S., and Williams, K. D.: ESMValTool (v1.0) – a community diagnostic and performance metrics tool for routine evaluation of Earth system models in CMIP, Geosci. Model Dev., 9, 1747-1802, 10.5194/gmd-9-1747-2016, 2016.

Fast, J. D., Berg, L. K., Alexander, L., Bell, D., D'Ambro, E., Hubbe, J., Kuang, C., Liu, J., Long, C., Matthews, A., Mei, F., Newsom, R., Pekour, M., Pinterich, T., Schmid, B., Schobesberger, S., Shilling, J., Smith, J. N., Springston, S., Suski, K., Thornton, J. A., Tomlinson, J., Wang, J., Xiao, H., and Zelenyuk, A.: Overview of the HI-SCALE Field Campaign: A New Perspective on Shallow Convective Clouds, Bull. Amer. Meteor. Soc., 100, 821-840, 10.1175/bams-d-18-0030.1, 2019.

Gallo, F., Uin, J., Springston, S., Wang, J., Zheng, G., Kuang, C., Wood, R., Azevedo, E. B., McComiskey, A., Mei, F., Theisen, A., Kyrouac, J., and Aiken, A. C.: Identifying a regional aerosol baseline in the eastern North Atlantic using collocated measurements and a mathematical algorithm to mask high-submicron-number-concentration aerosol events, Atmos. Chem. Phys., 20, 7553-7573, 10.5194/acp-20-7553-2020, 2020.

Gelaro, R., McCarty, W., Suarez, M. J., Todling, R., Molod, A., Takacs, L., Randles, C., Darmenov, A., Bosilovich, M. G., Reichle, R., Wargan, K., Coy, L., Cullather, R., Draper, C., Akella, S., Buchard, V., Conaty, A., da Silva, A., Gu, W., Kim, G. K., Koster, R., Lucchesi, R., Merkova, D., Nielsen, J. E., Partyka, G., Pawson, S., Putman, W., Rienecker, M., Schubert, S. D., Sienkiewicz, M., and Zhao, B.: The Modern-Era Retrospective Analysis for Research and Applications, Version 2 (MERRA-2), J. Climate, 30, 5419-5454, 10.1175/JCLI-D-16-0758.1, 2017.

Glassmeier, F., Hoffmann, F., Johnson, J. S., Yamaguchi, T., Carslaw, K. S., and Feingold, G.: An emulator approach to stratocumulus susceptibility, Atmos. Chem. Phys., 19, 10191-10203, 10.5194/acp-19-10191-2019, 2019.

Gleckler, P. J., Doutriaux, C., Durack, P. J., Taylor, K. E., Zhang, Y., Williams, D. N., Mason, E., and Servonnat, J.: A more powerful reality test for climate models, Eos, Trans. Amer. Geophys. Union, 97, 10.1029/2016EO051663, 2016.

Golaz, J.-C., Van Roekel, L. P., Zheng, X., Roberts, A. F., Wolfe, J. D., Lin, W., Bradley, A. M., Tang, Q., Maltrud, M. E., Forsyth, R. M., Zhang, C., Zhou, T., Zhang, K., Zender, C. S., Wu, M., Wang, H., Turner, A. K., Singh, B., Richter, J. H., Qin, Y., Petersen, M. R., Mametjanov, A., Ma, P.-L., Larson, V. E., Krishna, J., Keen, N. D., Jeffery, N., Hunke, E. C., Hannah, W. M., Guba, O., Griffin, B. M., Feng, Y., Engwirda, D., Di Vittorio, A. V., Dang, C., Conlon, L. M., Chen, C.-C.-J., Brunke, M. A., Bisht, G., Benedict, J. J., Asay-Davis, X. S., Zhang, Y., Zhang, M., Zeng, X., Xie, S., Wolfram, P. J., Vo, T., Veneziani, M., Tesfa, T. K., Sreepathi, S., Salinger, A. G., Jack Reeves Eyre, J. E., Prather, M. J., Mahajan, S., Li, Q., Jones, P. W., Jacob, R. L., Huebler, G. W., Huang, X., Hillman, B. R., Harrop, B. E., Foucar, J. G., Fang, Y., Comeau, D. S., Caldwell, P. M., Bartoletti, T., Balaguru, K., Taylor, M. A., McCoy, R. B., Leung, L. R., and Bader, D. C.: The DOE E3SM Model Version 2: Overview of the physical model and initial model evaluation, Journal of Advances in Modeling Earth Systems, n/a, e2022MS003156, 10.1029/2022MS003156, 2022.

Golaz, J.-C., Caldwell, P. M., Van Roekel, L. P., Petersen, M. R., Tang, Q., Wolfe, J. D., Abeshu, G., Anantharaj, V., Asay-Davis, X. S., Bader, D. C., Baldwin, S. A., Bisht, G., Bogenschutz, P. A., Branstetter, M., Brunke, M. A., Brus, S. R., Burrows, S. M., Cameron-Smith, P. J., Donahue, A. S., Deakin, M., Easter, R. C., Evans, K. J., Feng, Y., Flanner, M., Foucar, J. G., Fyke, J. G., Griffin, B. M., Hannay, C., Harrop, B. E., Hoffman, M. J., Hunke, E. C., Jacob, R. L., Jacobsen, D. W., Jeffery, N., Jones, P. W., Keen, N. D., Klein, S. A., Larson, V. E., Leung, L. R., Li, H.-Y., Lin, W., Lipscomb, W. H., Ma, P.-L., Mahajan, S., Maltrud, M. E., Mametjanov, A., McClean, J. L., McCoy, R. B., Neale, R. B., Price, S. F., Qian, Y., Rasch, P. J., Reeves Eyre, J. E. J., Riley, W. J., Ringler, T. D., Roberts, A. F., Roesler, E. L., Salinger, A. G., Shaheen, Z., Shi, X., Singh, B., Tang, J., Taylor, M. A., Thornton, P. E., Turner, A. K., Veneziani, M., Wan, H., Wang, H., Wang, S., Williams, D. N., Wolfram, P. J., Worley, P. H., Xie, S., Yang, Y., Yoon, J.-H., Zelinka, M. D., Zender, C. S., Zeng, X., Zhang, C., Zhang, K., Zhang, Y., Zheng, X., Zhou, T., and Zhu, Q.: The DOE E3SM Coupled Model Version 1: Overview and Evaluation at Standard Resolution, J. Adv. Model. Earth Syst., 11, 2089-2129, 10.1029/2018ms001603, 2019.

Grosvenor, D. P., Sourdeval, O., Zuidema, P., Ackerman, A., Alexandrov, M. D., Bennartz, R., Boers, R., Cairns, B., Chiu, J. C., Christensen, M., Deneke, H., Diamond, M., Feingold, G., Fridlind, A., Hünerbein, A., Knist, C., Kollias, P., Marshak, A., McCoy, D., Merk, D., Painemal, D., Rausch, J., Rosenfeld, D., Russchenberg, H., Seifert, P., Sinclair, K., Stier, P., van Diedenhoven, B., Wendisch, M., Werner, F., Wood, R., Zhang, Z., and Quaas, J.: Remote Sensing of Droplet Number Concentration in Warm Clouds: A Review of the Current State of Knowledge and Perspectives, Reviews of Geophysics, 56, 409-453, 10.1029/2017RG000593, 2018.

Gryspeerdt, E., Goren, T., Sourdeval, O., Quaas, J., Mülmenstädt, J., Dipu, S., Unglaub, C., Gettelman, A., and Christensen, M.: Constraining the aerosol influence on cloud liquid water path, Atmos. Chem. Phys., 19, 5331-5347, 10.5194/acp-19-5331-2019, 2019.

Gryspeerdt, E., Mülmenstädt, J., Gettelman, A., Malavelle, F. F., Morrison, H., Neubauer, D., Partridge, D. G., Stier, P., Takemura, T., Wang, H., Wang, M., and Zhang, K.: Surprising similarities in model and observational aerosol radiative forcing estimates, Atmos. Chem. Phys., 20, 613-623, 10.5194/acp-20-613-2020, 2020.

Humphries, R.: MARCUS ARM CN and CCN data reprocessed to remove ship exhaust influence (v2) [dataset], 10.25919/ezp0-em87, 2020.

Humphries, R. S., McRobert, I. M., Ponsonby, W. A., Ward, J. P., Keywood, M. D., Loh, Z. M., Krummel, P. B., and Harnwell, J.: Identification of platform exhaust on the RV Investigator, Atmos. Meas. Tech., 12, 3019-3038, 10.5194/amt-12-3019-2019, 2019.

IPCC: Climate Change 2021: The Physical Science Basis. Contribution of Working Group I to the Sixth Assessment Report of the Intergovernmental Panel on Climate Change, Cambridge University Press, Cambridge, United Kingdom and New York, NY, USA, 2391 pp., 10.1017/9781009157896, 2021.

Jiang, X., Lau, N.-C., and Klein, S. A.: Role of eastward propagating convection systems in the diurnal cycle and seasonal mean of summertime rainfall over the U.S. Great Plains, Geophys. Res. Lett., 33, 10.1029/2006gl027022, 2006.

Lewis, E. R. and Teixeira, J.: Dispelling clouds of uncertainty, Eos, Trans. Amer. Geophys. Union, 96, 10.1029/2015eo031303, 2015.

Lim, K.-S. S., Riihimaki, L., Comstock, J. M., Schmid, B., Sivaraman, C., Shi, Y., and McFarquhar, G. M.: Evaluation of long-term surface-retrieved cloud droplet number concentration with in situ aircraft observations, Journal of Geophysical Research: Atmospheres, 121, 2318-2331, 10.1002/2015JD024082, 2016.

Ma, P. L., Harrop, B. E., Larson, V. E., Neale, R. B., Gettelman, A., Morrison, H., Wang, H., Zhang, K., Klein, S. A., Zelinka, M. D., Zhang, Y., Qian, Y., Yoon, J. H., Jones, C. R., Huang, M., Tai, S. L., Singh, B., Bogenschutz, P. A., Zheng, X., Lin, W., Quaas, J., Chepfer, H., Brunke, M. A., Zeng, X., Mülmenstädt, J., Hagos, S., Zhang, Z., Song, H., Liu, X., Pritchard, M. S., Wan, H., Wang, J., Tang, Q., Caldwell, P. M., Fan, J., Berg, L. K., Fast, J. D., Taylor, M. A., Golaz, J. C., Xie, S., Rasch, P. J., and Leung, L. R.: Better calibration of cloud parameterizations and subgrid effects increases the fidelity of the E3SM Atmosphere Model version 1, Geosci. Model Dev., 15, 2881-2916, 10.5194/gmd-15-2881-2022, 2022.

Maloney, E. D., Gettelman, A., Ming, Y., Neelin, J. D., Barrie, D., Mariotti, A., Chen, C. C., Coleman, D. R. B., Kuo, Y.-H., Singh, B., Annamalai, H., Berg, A., Booth, J. F., Camargo, S. J., Dai, A., Gonzalez, A., Hafner, J., Jiang, X., Jing, X., Kim, D., Kumar, A., Moon, Y., Naud, C. M., Sobel, A. H., Suzuki, K., Wang, F., Wang, J., Wing, A. A., Xu, X., and Zhao, M.: Process-Oriented Evaluation of Climate and Weather Forecasting Models, Bull. Amer. Meteor. Soc., 100, 1665-1686, 10.1175/bams-d-18-0042.1, 2019.

McFarquhar, G. M., Bretherton, C. S., Marchand, R., Protat, A., DeMott, P. J., Alexander, S. P., Roberts, G. C., Twohy, C. H., Toohey, D., Siems, S., Huang, Y., Wood, R., Rauber, R. M., Lasher-Trapp, S., Jensen, J., Stith, J. L., Mace, J., Um, J., Järvinen, E., Schnaiter, M., Gettelman, A., Sanchez, K. J., McCluskey, C. S., Russell, L. M., McCoy, I. L., Atlas, R. L., Bardeen, C. G., Moore, K. A., Hill, T. C. J., Humphries, R. S., Keywood, M. D., Ristovski, Z., Cravigan, L., Schofield, R., Fairall, C., Mallet, M. D., Kreidenweis, S. M., Rainwater, B., D'Alessandro, J., Wang, Y., Wu, W., Saliba, G., Levin, E. J. T., Ding, S., Lang, F., Truong, S. C. H., Wolff, C., Haggerty, J., Harvey, M. J., Klekociuk, A. R., and McDonald, A.: Observations of Clouds, Aerosols, Precipitation, and Surface Radiation over the Southern Ocean: An Overview of CAPRICORN, MARCUS, MICRE, and SOCRATES, Bull. Amer. Meteor. Soc., 102, E894-E928, 10.1175/bams-d-20-0132.1, 2021.

Min, Q. and Harrison, L. C.: Cloud properties derived from surface MFRSR measurements and comparison with GOES results at the ARM SGP Site, Geophysical Research Letters, 23, 1641-1644, 10.1029/96GL01488, 1996.

Minnis, P., Nguyen, L., Palikonda, R., Heck, P. W., Spangenberg, D. A., Doelling, D. R., Ayers, J. K., Smith, J. W. L., Khaiyer, M. M., Trepte, Q. Z., Avey, L. A., Chang, F.-L., Yost, C. R., Chee, T. L., and Szedung, S.-M.: Near-real time cloud retrievals from operational and research meteorological satellites, Proc. SPIE Europe Remote Sens., Cardiff, Wales, UK,, 15-18 September, 710703, 10.1117/12.800344, 2008.

Minnis, P., Sun-Mack, S., Young, D. F., Heck, P. W., Garber, D. P., Chen, Y., Spangenberg, D. A., Arduini, R. F., Trepte, Q. Z., Smith, W. L., Ayers, J. K., Gibson, S. C., Miller, W. F., Hong, G., Chakrapani, V., Takano, Y., Liou, K. N., Xie, Y., and Yang, P.: CERES Edition-2 Cloud Property Retrievals Using TRMM VIRS and Terra and Aqua MODIS Data—Part I: Algorithms, IEEE Transactions on Geoscience and Remote Sensing, 49, 4374-4400, 10.1109/TGRS.2011.2144601, 2011.

Myhre, G., Samset, B. H., Schulz, M., Balkanski, Y., Bauer, S., Berntsen, T. K., Bian, H., Bellouin, N., Chin, M., Diehl, T., Easter, R. C., Feichter, J., Ghan, S. J., Hauglustaine, D., Iversen, T., Kinne, S., Kirkevåg, A., Lamarque, J. F., Lin, G., Liu, X., Lund, M. T., Luo, G., Ma, X., van Noije, T., Penner, J. E., Rasch, P. J., Ruiz, A., Seland, Ø., Skeie, R. B., Stier, P., Takemura, T., Tsigaridis, K., Wang, P., Wang, Z., Xu, L., Yu, H., Yu, F., Yoon, J. H., Zhang, K., Zhang, H., and Zhou, C.: Radiative forcing of the direct aerosol effect from AeroCom Phase II simulations, Atmos. Chem. Phys., 13, 1853-1877, 10.5194/acp-13-1853-2013, 2013.

NETCDF: Introduction and Overview: https://www.unidata.ucar.edu/software/netcdf/docs/index.html, last access: 12 November 2022.

Quaas, J., Boucher, O., Bellouin, N., and Kinne, S.: Satellite-based estimate of the direct and indirect aerosol climate forcing, Journal of Geophysical Research: Atmospheres, 113, 10.1029/2007JD008962, 2008.

Quaas, J., Ming, Y., Menon, S., Takemura, T., Wang, M., Penner, J. E., Gettelman, A., Lohmann, U., Bellouin, N., Boucher, O., Sayer, A. M., Thomas, G. E., McComiskey, A., Feingold, G., Hoose, C., Kristjánsson, J. E., Liu, X., Balkanski, Y., Donner, L. J., Ginoux, P. A., Stier, P., Grandey, B., Feichter, J., Sednev, I., Bauer, S. E., Koch, D., Grainger, R. G., Kirkev, aring, g, A., Iversen, T., Seland, Ø., Easter, R., Ghan, S. J., Rasch, P. J., Morrison, H., Lamarque, J. F., Iacono, M. J., Kinne, S., and Schulz, M.: Aerosol indirect effects – general circulation model intercomparison and evaluation with satellite data, Atmos. Chem. Phys., 9, 8697-8717, 10.5194/acp-9-8697-2009, 2009.

Rasch, P. J., Xie, S., Ma, P.-L., Lin, W., Wang, H., Tang, Q., Burrows, S. M., Caldwell, P., Zhang, K., Easter, R. C., Cameron-Smith, P., Singh, B., Wan, H., Golaz, J.-C., Harrop, B. E., Roesler, E., Bacmeister, J., Larson, V. E., Evans, K. J., Qian, Y., Taylor, M., Leung, L. R., Zhang, Y., Brent, L., Branstetter, M., Hannay, C., Mahajan, S., Mametjanov, A., Neale, R., Richter, J. H., Yoon, J.-H., Zender, C. S., Bader, D., Flanner, M., Foucar, J. G., Jacob, R., Keen, N., Klein, S. A., Liu, X., Salinger, A. G., Shrivastava, M., and Yang, Y.: An Overview of the Atmospheric Component of the Energy Exascale Earth System Model, J. Adv. Model. Earth Syst., 11, 2377-2411, 10.1029/2019ms001629, 2019.

Reddington, C. L., Carslaw, K. S., Stier, P., Schutgens, N., Coe, H., Liu, D., Allan, J., Browse, J., Pringle, K. J., Lee, L. A., Yoshioka, M., Johnson, J. S., Regayre, L. A., Spracklen, D. V., Mann, G. W., Clarke, A., Hermann, M., Henning, S., Wex, H., Kristensen, T. B., Leaitch, W. R., Pöschl, U., Rose, D., Andreae, M. O., Schmale, J., Kondo, Y., Oshima, N., Schwarz, J. P., Nenes, A., Anderson, B., Roberts, G. C., Snider, J. R., Leck, C., Quinn, P. K., Chi, X., Ding, A., Jimenez, J. L., and Zhang, Q.: The Global Aerosol Synthesis and Science Project (GASSP): Measurements and Modeling to Reduce Uncertainty, Bull. Amer. Meteor. Soc., 98, 1857-1877, 10.1175/bams-d-15-00317.1, 2017.

Riihimaki, L., McFarlane, S., and Sivaraman, C.: Droplet Number Concentration Value-Added Product, ARM Research FacilityDOE/SC-ARM-TR-140, 2021.

Schulz, M., Textor, C., Kinne, S., Balkanski, Y., Bauer, S., Berntsen, T., Berglen, T., Boucher, O., Dentener, F., Guibert, S., Isaksen, I. S. A., Iversen, T., Koch, D., Kirkevåg, A., Liu, X., Montanaro, V., Myhre, G., Penner, J. E., Pitari, G., Reddy, S., Seland, Ø., Stier, P., and Takemura, T.: Radiative forcing by aerosols as derived from the AeroCom present-day and pre-industrial simulations, Atmos. Chem. Phys., 6, 5225-5246, 10.5194/acp-6-5225-2006, 2006.

Song, X., Zhang, G. J., and Li, J. L. F.: Evaluation of Microphysics Parameterization for Convective Clouds in the NCAR Community Atmosphere Model CAM5, J. Climate, 25, 8568-8590, 10.1175/JCLI-D-11-00563.1, 2012.

Sun, J., Zhang, K., Wan, H., Ma, P.-L., Tang, Q., and Zhang, S.: Impact of Nudging Strategy on the Climate Representativeness and Hindcast Skill of Constrained EAMv1 Simulations, J. Adv. Model. Earth Syst., 11, 3911-3933, 10.1029/2019MS001831, 2019.

Tang, Q., Klein, S. A., Xie, S., Lin, W., Golaz, J. C., Roesler, E. L., Taylor, M. A., Rasch, P. J., Bader, D. C., Berg, L. K., Caldwell, P., Giangrande, S. E., Neale, R. B., Qian, Y., Riihimaki, L. D., Zender, C. S., Zhang, Y., and Zheng, X.: Regionally refined test bed in E3SM atmosphere model version 1 (EAMv1) and applications for high-resolution modeling, Geosci. Model Dev., 12, 2679-2706, 10.5194/gmd-12-2679-2019, 2019.

Tang, S., Zhang, M., and Xie, S.: An ensemble constrained variational analysis of atmospheric forcing data and its application to evaluate clouds in CAM5, J. Geophys. Res. Atmos., 121, 33-48, 10.1002/2015JD024167, 2016.

Tang, S., Gleckler, P., Xie, S., Lee, J., Ahn, M.-S., Covey, C., and Zhang, C.: Evaluating the Diurnal and Semidiurnal Cycle of Precipitation in CMIP6 Models Using Satellite- and Ground-Based Observations, J. Climate, 34, 3189-3210, 10.1175/jcli-d-20-0639.1, 2021.

Tang, S., Fast, J. D., Zhang, K., Hardin, J. C., Varble, A. C., Shilling, J. E., Mei, F., Zawadowicz, M. A., and Ma, P. L.: Earth System Model Aerosol–Cloud Diagnostics (ESMAC Diags) package, version 1: assessing E3SM aerosol predictions using aircraft, ship, and surface measurements, Geosci. Model Dev., 15, 4055-4076, 10.5194/gmd-15-4055-2022, 2022a.

Tang, S., Xie, S., Guo, Z., Hong, S.-Y., Khouider, B., Klocke, D., Köhler, M., Koo, M.-S., Krishna, P. M., Larson, V. E., Park, S., Vaillancourt, P. A., Wang, Y.-C., Yang, J., Daleu, C. L., Homeyer, C. R., Jones, T. R., Malap, N., Neggers, R., Prabhakaran, T., Ramirez, E., Schumacher, C., Tao, C., Bechtold, P., Ma, H.-Y., Neelin, J. D., and Zeng, X.: Long-term single-column model intercomparison of diurnal cycle of precipitation over midlatitude and tropical land, Quarterly Journal of the Royal Meteorological Society, 148, 641-669, 10.1002/qj.4222, 2022b.

Turner, D. D., Lo, C., Min, Q., Zhang, D., and Gaustad, K.: Cloud Optical Properties from the Multifilter Shadowband Radiometer (MFRSRCLDOD): An ARM Value-Added Product, ARM Research FacilityDOE/SC-ARM-TR-047, 2021.

Varble, A. C., Ma, P. L., Christensen, M. W., Mülmenstädt, J., Tang, S., and Fast, J.: Evaluation of Liquid Cloud Albedo Susceptibility in E3SM Using Coupled Eastern North Atlantic Surface and Satellite Retrievals, EGUsphere, 2023, 1-39, 10.5194/egusphere-2023-998, 2023.

Wang, J., Wood, R., Jensen, M. P., Chiu, J. C., Liu, Y., Lamer, K., Desai, N., Giangrande, S. E., Knopf, D. A., Kollias, P., Laskin, A., Liu, X., Lu, C., Mechem, D., Mei, F., Starzec, M., Tomlinson, J., Wang, Y., Yum, S. S., Zheng, G., Aiken, A. C., Azevedo, E. B., Blanchard, Y., China, S., Dong, X., Gallo, F., Gao, S., Ghate, V. P., Glienke, S., Goldberger, L., Hardin, J. C., Kuang, C., Luke, E. P., Matthews, A. A., Miller, M. A., Moffet, R., Pekour, M., Schmid, B., Sedlacek, A. J., Shaw, R. A., Shilling, J. E., Sullivan, A., Suski, K., Veghte, D. P., Weber, R., Wyant, M., Yeom, J., Zawadowicz, M., and Zhang, Z.: Aerosol and Cloud Experiments in the Eastern North Atlantic (ACE-ENA), Bull. Amer. Meteor. Soc., 1-51, 10.1175/bams-d-19-0220.1, 2021.

Watson-Parris, D., Schutgens, N., Reddington, C., Pringle, K. J., Liu, D., Allan, J. D., Coe, H., Carslaw, K. S., and Stier, P.: In situ constraints on the vertical distribution of global aerosol, Atmos. Chem. Phys., 19, 11765-11790, 10.5194/acp-19-11765-2019, 2019.

Wu, P., Dong, X., Xi, B., Tian, J., and Ward, D. M.: Profiles of MBL Cloud and Drizzle Microphysical Properties Retrieved From Ground-Based Observations and Validated by Aircraft In Situ Measurements Over the Azores, Journal of Geophysical Research: Atmospheres, 125, e2019JD032205, 10.1029/2019JD032205, 2020.

Xie, S., Lin, W., Rasch, P. J., Ma, P.-L., Neale, R., Larson, V. E., Qian, Y., Bogenschutz, P. A., Caldwell, P., Cameron-Smith, P., Golaz, J.-C., Mahajan, S., Singh, B., Tang, Q., Wang, H., Yoon, J.-H., Zhang, K., and Zhang, Y.: Understanding Cloud and Convective Characteristics in Version 1 of the E3SM Atmosphere Model, J. Adv. Model. Earth Syst., 10, 2618-2644, 10.1029/2018MS001350, 2018.

Xu, K.-M. and Cheng, A.: Evaluating Low-Cloud Simulation from an Upgraded Multiscale Modeling Framework Model. Part II: Seasonal Variations over the Eastern Pacific, J. Climate, 26, 5741-5760, 10.1175/JCLI-D-12-00276.1, 2013a.

Xu, K.-M. and Cheng, A.: Evaluating Low-Cloud Simulation from an Upgraded Multiscale Modeling Framework Model. Part I: Sensitivity to Spatial Resolution and Climatology, J. Climate, 26, 5717-5740, 10.1175/JCLI-D-12-00200.1, 2013b.

Zhang, C., Xie, S., Tao, C., Tang, S., Emmenegger, T., Neelin, J. D., Schiro, K. A., Lin, W., and Shaheen, Z.: The ARM Data-Oriented Metrics and Diagnostics Package for Climate Models: A New Tool for Evaluating Climate Models with Field Data, Bull. Amer. Meteor. Soc., 101, E1619-E1627, 10.1175/bams-d-19-0282.1, 2020.

Zhang, S., Zhang, K., Wan, H., and Sun, J.: Further improvement and evaluation of nudging in the E3SM Atmosphere Model version 1 (EAMv1): simulations of the mean climate, weather events, and anthropogenic aerosol effects, Geosci. Model Dev., 15, 6787-6816, 10.5194/gmd-15-6787-2022, 2022.

Zhang, Y., Xie, S., Lin, W., Klein, S. A., Zelinka, M., Ma, P.-L., Rasch, P. J., Qian, Y., Tang, Q., and Ma, H.-Y.: Evaluation of Clouds in Version 1 of the E3SM Atmosphere Model With Satellite Simulators, Journal of Advances in Modeling Earth Systems, 11, 1253-1268, 10.1029/2018MS001562, 2019.

Zhou, X., Kollias, P., and Lewis, E. R.: Clouds, Precipitation, and Marine Boundary Layer Structure during the MAGIC Field Campaign, J. Climate, 28, 2420-2442, 10.1175/jcli-d-14-00320.1, 2015.